JWST/NIRSpec reveals the atmospheric driver of Saturn's variable magnetospheric rotation rate

Tom S. Stallard[1], Luke Moore[2], Henrik Melin[1], Chris G. A. Smith[3], Omakshi Agiwal[2], M. Nahid Chowdhury[4], Rosie E. Johnson[5], Katie L. Knowles[1], Emma M. Thomas[1], Paola I. Tiranti[1], James O'Donoghue[6], Khalid Mohamed[2], Ingo Mueller-Wodarg[7], John C. Coxon[1], Sarah V. Badman[8], Joe A. Caggiano[9]

[1]Department of Maths, Physics, and Electrical Engineering, Northumbria University, Newcastle Upon Tyne, UK
[2]Center for Space Physics, Boston University, Boston, MA, USA
[3]Huddersfield New College, New Hey Road, Huddersfield, HD3 4GL, United Kingdom
[4]School of Physics and Astronomy, University of Leicester, Leicester, UK
[5]Department of Physics, Aberystwyth University, Aberystwyth, UK
[6]Space and Atmospheric Electricity Group, Department of Meteorology, Reading, UK
[7]Blackett Laboratory, Imperial College London, London, UK
[8]Physics Department, Lancaster University, Lancaster, UK
[9]Solar and Space Physics Group, Johns Hopkins University Applied Physics Laboratory, Laurel, USA

Key Points:

- Temperatures and H_3^+ densities of Saturn's auroral ionosphere mapped in detail for the first time, at unprecedented sensitivity
- Both temperature and density contain centrally inverted pairs of maximum and minimum values, indicators of the planetary period current
- The H_3^+ density peak is collocated with the heat source from past modeling, suggesting magnetospheric feedback may drive these currents

Corresponding author: Tom S. Stallard, tom.stallard@northumbria.ac.uk

Abstract

Past measurements of Saturn's upper atmosphere have allowed only a broad scale view of the temperature and ion density structures within the auroral region. However, Saturn's auroral currents include a planetary period current component that is produced by neutral atmospheric flows. In order to understand the ultimate source for Saturn's planetary period aurora, we need vastly improved measurements of Saturn's auroral region. Here, using the first JWST/NIRSpec observations of Saturn, we reveal incredibly high spatial resolution (<500 km/pixel) views of Saturn's auroral region for the first time. This provides at least an order-of-magnitude improvement in our measurement of the temperature and column density structure within Saturn's auroral region. It reveals an auroral region at the time of observation that is highly controlled by the planetary period currents, resulting in a series of upwards and downward currents from the pole to below the main auroral region. These are paired with reflected and inverted regions of heating and cooling across the auroral region. These patterns match surprisingly well to past model predictions, suggesting both the changes in column density and temperature are the direct result of localized heating positioned over the region of strongest particle precipitation. This strongly indicates that the planetary period currents are produced by a feedback loop, powered by the energy of magnetospherically generated aurora, preferentially heating one side of the auroral region.

Plain Language Summary

Saturn's ionosphere has been notoriously difficult to observe. Our best tool to remotely measure the upper-most layers of Saturn's atmosphere is to measure the glow from an ionic molecule called trihydrogen cation. This molecule is heated by Saturn's thermosphere, and so glows brightly, allowing us to directly measure the ionosphere from Earth. However, in contrast with Jupiter's very hot thermosphere, the moderate temperatures in Saturn's upper atmosphere have always made detailed measurements very challenging. Here, we use JWST observations of the trihydrogen cation at Saturn to revolutionize our understanding of this layer of the atmosphere. In incredible detail, we reveal complex temperature and density structures across this region that are very highly ordered, with rotating regions of heating and cooling. These regions are very similar to previously published models, indicating that Saturn's unique 'atmosphere-driven' aurora is self-sustained, powered like a heat pump, draining energy from the magnetosphere.

1 Introduction

There is little direct information about how energy flows into and through the upper atmosphere of Saturn, unlike both Jupiter and Uranus, where plentiful measurements of the ionospheric temperatures have been made over several decades. Jupiter's aurorae strongly control the atmospheric temperatures observed in both the auroral upper atmosphere (Stallard et al., 2002), as well as the powering heating deeper within the underlying stratosphere (Melin et al., 2006; Sinclair et al., 2023) and transporting heat equatorward through the thermosphere (Yates et al., 2020; O'Donoghue et al., 2021, 2025; Roberts et al., 2025). While the drivers of heat within Uranus's thermosphere are more controversial, we do have detailed measurements of the upper atmospheric temperature, which has been steadily declining for unknown reasons, since Voyager II visited the planet in 1986 (Melin et al., 2011; Melin, 2020).

At the heart of many of these observations is the use of at least moderate-resolution spectroscopy to measure the ro-vibrational temperatures of the molecular ion H_3^+ within a planet's ionosphere. These ions are typically embedded within the surrounding thermosphere, and so are quasi-thermalized (Miller et al., 1990), such that measurements of the relative brightness of different ro-vibrational lines of H_3^+ can provide the observer with a proxy for the temperature of the surrounding thermosphere (Drossart et al., 1989).

In contrast with this, Saturn's auroral temperatures have remained poorly constrained (Miller et al., 2020). Ground-based observations of the auroral region have the advantage of very high spectral resolution, allowing Saturn's rich background of reflected sunlight and non-ionospheric emissions to be better accounted for, but the relative weakness of Saturn's ionospheric emission makes resolving spatial details difficult. Stallard et al. (2019) provides a highly-smoothed local time averaged northern temperature map (combining seven nights of Keck data) with temperatures ranging between 350-450 K. While in line with past measurements which smoothed over significant latitude and/or longitudinal regions (527 K, 418 K and 361 K from O'Donoghue et al., 2014, 2016 and Chowdhury, Stallard, Melin, & Johnson, 2019 respectively), on individual nights, Stallard et al. (2019)'s temperature maps covered much wider ranges, between 250-650 K.

Similarly, Cassini's Visible and Infrared Mapping Spectrometer (VIMS) measurements of auroral temperatures were able to resolve small-scale features well, including regions above the limb (567-611 K; Stallard, Melin, Miller, O'Donoghue, et al., 2012) and within the main oval itself (440 K; Melin et al., 2011), but on larger scales struggled with background subtraction, due to the low spectral resolution of VIMS (Miller et al., 2020), so that published temperature maps again measured very large temperature ranges between 200-800 K (Lamy et al., 2013). Cassini Ultraviolet Imaging Spectrograph (UVIS) occultation observations of the exosphere also provide good measures of the upper atmospheric temperatures (380-590 K across all latitudes; Koskinen et al., 2015), with auroral temperatures showing significant variability, decreasing from ∼500 K at both 60°N and 60°S to ∼400 K at the pole (Brown et al., 2020). However, as point measurements, these again fail to provide anything other than time-averaged spatial information across the planetary disk. As a result, since the detection of H_3^+ at Saturn in 1992 (Geballe et al., 1993), neither ground or space based instrumentation has been able to properly resolve spatial variations in the physical parameters of Saturn's auroral region.

Equally, infrared measurements have struggled to tightly constrain the H_3^+ densities within the auroral ionosphere, since these calculations rely upon temperatures, resulting in column densities between 1-2$\times10^{15}$ m^{-2} (O'Donoghue et al., 2014), 2-8$\times10^{15}$ m^{-2} (Chowdhury et al., 2019) and 5-30$\times10^{15}$ m^{-2} (O'Donoghue et al., 2016), with Stallard et al. (2019)'s column densities effectively measuring noise. Cassini-VIMS provided a constraint on a very narrow segment of the main aurora at 7$\times10^{15}$ m^{-2}, but failed to map column densities across the entire auroral region (Lamy et al., 2013).

The poor constraints on Saturn's auroral temperatures are particularly noteworthy, because uniquely within the solar system, Saturn's main auroral oval is thought to be driven, in part, by atmospheric winds. This main auroral emission is generated by two separate processes (Hunt et al., 2014):

The first type of aurora, observed to be highly local time dependent, is poorly constrained in detail, but is produced through '*sub-corotation currents*' resulting from a combination of interactions between the magnetosphere and solar wind. The likely source is driving currents within the middle magnetosphere (Bunce et al., 2008; Hunt et al., 2014), perhaps a Saturnian Vasyliunas-cycle equivalent (Vasyliunas, 1983) to the Earth's Dungey-cycle aurora (Dungey, 1961), evidence of which has been observed in Saturn's dawn region (Hunt et al., 2022). This is believed to be an approximately axisymmetric current system producing upward currents around ∼75°N, though the aurora is typically brighter at dusk (Bader et al., 2019). However, changes in solar wind conditions drive dramatic enhancements in the auroral brightness and morphology, with bright dawn aurora dominating (Bader et al., 2019; Clarke et al., 2009).

The second type of aurora, however, results from a super-imposed system of currents, locked with the approximate rotation rate of the planet, entering the auroral region on one side of the planet, flowing over the pole, then out at the other side. This sec-

ond '*planetary period*' auroral current is driven by thermospheric flows within the upper atmosphere (Chowdhury et al., 2022).

There are two results for the super-position of the sub-corotation and planetary period currents. Firstly, the aurora has a rotating region of bright and dim aurora that are observed remotely as a flashing pulse of kilometric radiation (Kaiser et al., 1980), where changes in the pulse-period were the origin of Saturn's changing radio measurements of the apparent rotation rate (Gurnett et al., 2007). Secondly, the planetary period currents from each polar ionospheric region (North and South) induce asymmetric components into the magnetosphere, resulting in variations in both magnetic fields (e.g. Andrews, Cowley, Dougherty, & Provan, 2010) and magnetospheric plasmas (e.g. Krupp et al., 2005), where the two phases constructively and destructively interact.

1.1 Saturn's planetary period auroral currents

The source of Saturn's planetary period auroral currents was once highly controversial (Carbary et al., 2018), but recent observations of Saturn's ionospheric winds (Chowdhury et al., 2022) and the changing location of magnetospheric currents (Hunt et al., 2014) have proven that these currents originate within the atmosphere of the planet, as modeled by Smith (2011) and Jia et al. (2012).

As highlighted in Figure 1a, these currents are the result of an as-yet unidentified neutral twin-cell vortex, rotating with a period close to a Saturnian day. This neutral twin-cell vortex partially accelerates ions in the ionosphere, but the incomplete acceleration of these ions results in an '*effective* $\boldsymbol{E}\times\boldsymbol{B}$ *ion drift*' (the ion drift within an electric $\mathbf{E}$ and magnetic $\mathbf{B}$ field, relative to the surrounding neutral atmosphere, with an effective ion drift occurring even when no electric field exists; Wang et al., 2023) in the opposite direction to the neutral twin-cell vortex. Collisions between neutrals and ions in this effective $\mathbf{E}\times\mathbf{B}$ ion drift then drives a perpendicular Pedersen current across the pole of the planet. This results in a current divergence on one side of the pole, thus producing field-aligned currents that flow out of the planet into the surrounding magnetosphere, and a current convergence at the other side of the planet, resulting in field-aligned currents closing from magnetosphere back into the planet (Smith, 2011; Jia et al., 2012).

As shown in Figure 1b and Figure 1c, these currents then flow along magnetic field lines, partially-closing within the magnetosphere, reducing their strength, and then closing within the hemispherically-opposite ionosphere in a weakened state (Hunt et al., 2014). These currents drive distortions within the magnetosphere, measured as periodic oscillations in the magnetic field, known as '*planetary period oscillations*', as well as numerous other changes across the magnetosphere, including the observed magnetospheric plasma density and velocity. As the field-aligned currents enter and leave each ionospheric hemisphere, they enhance and reduce sub-corotational auroral currents (the white and grey dotted regions in Fig 1a), driving an asymmetric rotating enhancement in the aurora in both poles, most notably the radio aurora.

This is important because radio pulses are typically used to measure a planet's internal rotation rate, including at Jupiter (Burke & Franklin, 1955), Uranus (Warwick et al., 1986) and Neptune (Warwick et al., 1989), as well as at other astrophysical objects including pulsars (Gold, 1968) and brown dwarfs (Yu et al., 2011). Uniquely then, as a result of the varying rotation of Saturn's two polar upper atmospheric regions, Saturn's magnetic field oscillation and radio auroral pulse are physically disconnected from the internal rotation rate, measured to be 10 h 32 m 45 s (Helled et al., 2015) using gravitational measurements or 10 h 33 m 38 s using ring seismology (Mankovich et al., 2019). In Saturn's northern polar region (and likely the southern polar region) they are also disconnected from the underlying troposphere, where the north pole hexagon and its associated eastward jet have rotated with a steady rotation period of 10 h 39 m 23 s, varying by only 3 seconds across the entire period from 1980 (Voyager 1) to 2014 (Cassini)

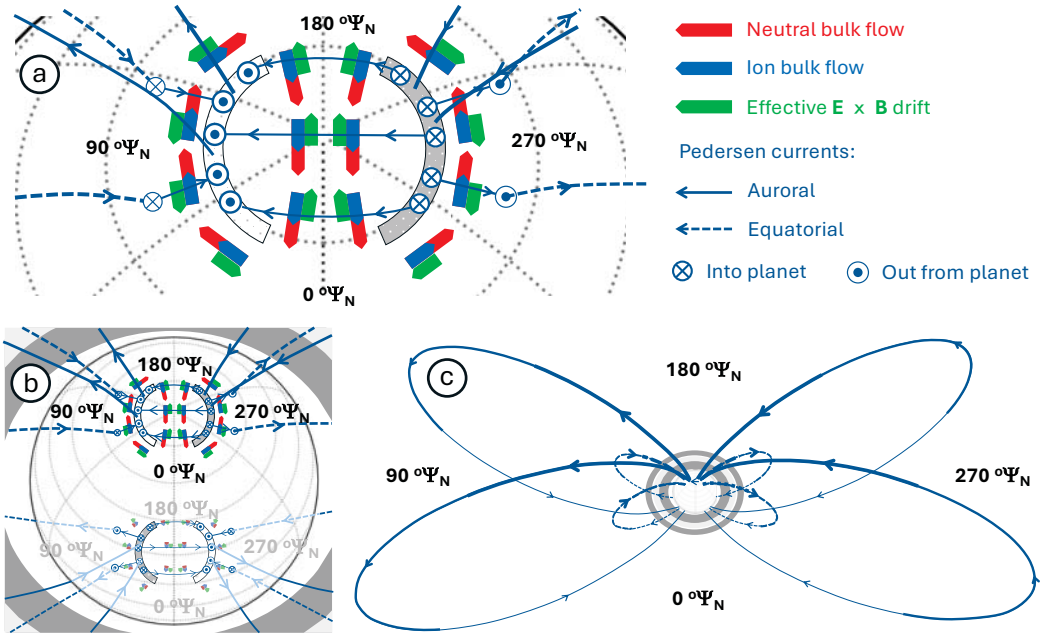

Figure 1. The northern planetary period current system. Panel a) shows twin-cell neutral vortex flows through the upper atmosphere (red block arrows), ineffectively accelerating the ionosphere bulk velocity (blue block arrows), resulting in an effective $\mathbf{E}\times\mathbf{B}$ ion drift in the opposite direction (with green block arrows showing the bulk flow of the ionosphere from the perspective of the co-located neutral atmosphere). Collisions between the ions and neutrals within this effective $\mathbf{E}\times\mathbf{B}$ ion drift results in a Pedersen current that flows perpendicular to this ion drift (blue line arrows). Currents flowing out of the planet (circle-dots) combine within the auroral region with the axi-symmetric sub-corotation currents, driving an enhancement in downwardly accelerated electrons, resulting in enhanced aurorae (white dotted region), while inwardly flowing currents (circle-crosses) mitigate the sub-corotation currents, resulting in reduced aurorae (grey dotted region). Equatorward of these auroral currents, ionospheric currents flow towards and away from the regions of divergence, originating closer to the equator from across the equatorial region, here represented by a single equatorward region of field aligned currents (dashed blue line arrows). Panel b) shows how the planetary period currents flow from one hemisphere (here, the North), to partially close in the other hemisphere (here the South). Note that in the figure, phase in the southern hemisphere is still given in Ψ_N, since it highlights currents driven by the northern twin-cell vortex closing into the south (independent of this, a separate current system driven within the southern polar region will also be driving currents in the Ψ_S phase). These weakened closing currents flow across the southern pole in the opposite direction to the North, but result in bulk neutral and ion flows in the same direction as in the North. This is possible, because the effective $\mathbf{E}\times\mathbf{B}$ ion drift is oppositely directed, with the ions powered externally from the other hemisphere moving more quickly, dragging the neutrals more slowly. Panel c) shows how the planetary period currents flow through the magnetosphere, weakening through partial closure within the magnetosphere before closing in the southern hemisphere. Notably, the matching planetary period current system originating in the southern auroral ionosphere (rotating in Ψ_S phase), and their driven closing currents in the northern hemisphere, are not shown.

(Sánchez-Lavega et al., 2014), an atmospheric feature that extends upwards 300 kilometers into the lower stratosphere (Fletcher et al., 2018).

This shows that the heat source that drives Saturn's twin-cell neutral vortex must originate from either the upper stratosphere or thermosphere. One possibility is that this energy source is localized as a single region of heating (Smith, 2011), resulting in a temperature difference within the neutral atmosphere that drives thermal winds across the auroral region. As these neutral winds flow, they drag ions within them, moving the charged ions across the planet's magnetic field, and thus inducing the planetary period current. Since this hot spot is entrained within the neutral atmosphere, this current rotates close to the internal rotation rate of the planet, but since no atmospheric layer is perfectly coupled with the underlying atmosphere, this layer can drift, resulting in a changing rotation rate, with different drift rates within each pole of the planet, producing the two different hemispheric periods of the planetary period current system (Gurnett et al., 2009).

1.2 Saturn's magnetospheric planetary periods

While it is the planetary period current system that drives these changes through the Saturnian system, measurements of these currents at the planet are incredibly challenging (Chowdhury et al., 2022), and cannot be used to constrain the rotational period of each ionosphere that drives them. As a result, measurements must be made outside the ionosphere, where the currents induced within the northern and southern ionosphere overlap to some degree, resulting in blending of the magnetic field variations (Provan et al., 2011) and auroral emission (Gurnett et al., 2009). However, despite these overlapping currents, the Cassini mission was able to take both radio (Kurth et al., 2008) and magnetometer (Andrews et al., 2008) measurements originating from each ionospheric hemisphere, producing two different rotational phases, one from the north and one from the south. Although broadly agreeing with one another, there were contrasts and contradictions between these phases.

Historically, for most of the Cassini mission, the '*planetary period oscillations*' observed by the magnetometer instrument were so clear that the resultant northern and southern phases could be easily identified (Andrews et al., 2008), resulting in a rotating coordinate system with which to frame both these magnetic oscillations and the currents that drive them. Defined in Hunt et al. (2014), in the southern planetary period phase Ψ_S, currents flow from the magnetosphere into the planet at $90°\Psi_S$ (reducing the sub-corotation currents, and weakening the electron accelerated aurora) and out from the planet (enhancing the sub-corotation currents, and brightening the electron accelerated aurora) at $270°\Psi_S$. These currents then flow into the surrounding magnetosphere, closing partially within the equatorial plasma and partly as a weaker interhemispheric current into the northern hemisphere. In the northern planetary period phase Ψ_N (Hunt et al., 2015), separate currents flow into the planet at $270°\Psi_N$ (reducing the sub-corotation currents) and out of the planet (enhancing the sub-corotation currents) at $90°\Psi_N$, again flowing through and partially closing within the magnetosphere, before closing in the southern hemisphere.

The two hemispheric phases Ψ_N and Ψ_S (and thus the rotation rates of the two upper atmospheres) are usually independent of one another, aligned with the observed Saturn Kilometric Radiation which also varies independently in each hemisphere. However, this independence is clearly reduced near the crossing of seasons. The Ulysses spacecraft measured an apparent convergence in the southern and northern periods in the years around the November 1995 equinox (Gurnett et al., 2010). Cassini's measurements of the Saturn Kilometric Radiation showed several convergencies in the rotation rate after the August 2009 equinox, with both hemispheres having similar periods and phases between March 2010 and February 2011, then again between August 2011 and June 2012 (Fischer et al., 2015).

In this same period, the magnetic field phases transitioned from pre-equinoctal values (where the rotational periods were very different) to much closer rotational periods as early as 2010, though unlike the radio periods, these did not fully converge until a relatively narrow period between mid-2013 and mid-2014, where the two phases were locked in antiphase (Provan et al., 2016). However, the broader period is also notable because of sudden and dramatic jumps in the magnetic phase every 100-200 days, with evidence these shifts occurred during periods of solar wind compression (Provan et al., 2015). The apparent contradictions between radio period and magnetic field phase have been suggested to result from the local time line-of-sight of Cassini's radio observations (Cowley & Provan, 2016).

After this, the radio periods of the two hemispheres once again diverged, and were observed to change independently until the end of the Cassini mission (Ye et al., 2016), with the northern period lengthening from 10.63 hours to 10.76 hours over four years, while the southern rotation remained relatively stable around 10.69 hours. The final measurements of these phases by Cassini, between the beginning of 2016 and the end of mission in mid-September 2017, showed a close alignment between the radio and magnetospheric periods, with a northern period of 10.79 hours and a southern period of 10.68 hours, both varying by only 0.01 hours (Provan, Lamy, et al., 2019). Notably, despite these relatively stable rotation rates, their associated errors over the seven year gap between 2017 and 2024 result in a complete loss of phase for each hemisphere. So significant is the uncertainty here, we estimate the error in the northern phase is >56 Saturnian days in 2024.

Notably, away from the equinoctial period, the rotational periods are slower in the summer hemisphere in the South before 2009 and the North after 2015, at around 10.8 hours and faster in the winter hemisphere, around 10.6 in the North before 2009 and 10.7 in the South after 2015. Brooks et al. (2019) argued that this was driven by the differential torque provided to the summer hemisphere as a result of enhanced conductivity in the sunlit ionosphere, which they predicted could drive a reduced overall rotation rate. Cowley et al. (2020) used magnetic field measurements to model these torques and showed that although (against the predictions of Brooks et al., 2019) the main auroral regions show comparable torques in both summer and winter, the polar open field line regions do show a strong torque asymmetry, suggesting a potential source for the slower rotation rates in summer. However, as will be discussed later and as noted by Cowley et al. (2020), the thermospheric rotation rates within the polar region are far slower than the planetary period of the current system, suggesting the source of this variable rotation rate is outside the polar and/or upper atmosphere.

In the Cassini Grand Finale, the dual modulation by the northern and southern planetary period current systems was found almost continuously across all mapped magnetic longitudes, including regions mapping to the rings (Provan, Cowley, Bradley, et al., 2019), though not within the D-ring region where azimuthal magnetic fields are thought to be driven by a separate equatorial inter-hemispheric current (Provan, Cowley, Bunce, et al., 2019). Notably, when correlated to the northern phase, the measured magnetic oscillation drifted with latitude from pole to equator, with the peak oscillation rotating by 90 degrees, from $90°\Psi_N$ in the auroral region to $0°\Psi_N$ near the equator. At the same time, the amplitude of the equatorial magnetic field oscillation was reduced down to approximately 1/3 the strength in the auroral regions (Provan, Cowley, Bradley, et al., 2019). There was also no evidence of the northern phase within the southern mid-latitudes, but the northern phase was clearly observed within the southern auroral regions. Interestingly, the same (rather than opposite) is true for the southern planetary period oscillation, also showing a drifting phase and reduced amplitude in the northern hemisphere and no signal in the southern hemisphere at mid-latitudes.

Measurements of the equatorial electron densities using the Cassini Radio and Plasma Wave Science instrument seem to align with this twisted planetary period current, show-

ing the highest electron densities at a northern phase of 0 $^{\circ}\Psi_N$ (Provan, Cowley, et al., 2021). If the equatorial phase is twisted by 90 degrees, as suggested by Provan, Cowley, Bradley, et al. (2019), this would place regions of enhanced electron densities within the equatorial downward field-aligned currents. Notably, these electron density measurements only observe a separation in electron density with planetary period above ∼2500 km, well above the H_3^+ emission layer, with electron densities below this matching across all planetary phases.

Closer to the planet's polar ionosphere, the dominance of the current system associated with each hemisphere's planetary period current becomes stronger, though not completely dominant. Both the auroral currents (Hunt et al., 2015) and emission brightness (Bader et al., 2018) include components from the planetary period currents of both hemispheres, with the auroral variation also being influenced, to a lesser extent, by both. In H_3^+ emission, the statistical northern aurorae varies by twice as much in the northern phase Ψ_N than when observed in the southern phase Ψ_S, and the statistical southern aurorae varies by three times as much in the southern phase as in the northern phase (Badman et al., 2012). In contrast with this, Chowdhury (2022) showed that while Saturn's northern ionospheric winds were strongly correlated to the northern phase, there were no clear southern phase correlations, suggesting the current closure associated with currents from the opposing hemisphere do not cleanly flow over the pole.

1.3 Origin for the atmospheric energy source

Although observations have resolved an atmospheric origin for Saturn's planetary period current, they have ultimately just moved the question to Saturn itself. The new question has become: "Where is the energy source that drives Saturn's planetary period current, and how does it produce this current?"

All theories for how neutral flows within Saturn's atmosphere drive currents out into the magnetosphere ultimately rely on collisional acceleration of the ionosphere, exchanging neutral momentum into ions that are forced to move perpendicularly through the surrounding magnetic field, driving ionospheric currents that then close within the surrounding magnetosphere.

Smith (2011) used a general circulation model to investigate the effect of arbitrary axially-asymmetric heating on the thermospheric winds, with the heat source fixed in longitude and at the latitude of the main auroral oval. This study demonstrated that such a model could qualitatively reproduce the main features of the observed planetary period currents. It produced a temperature contrast of about 15 K across the polar cap, leading to currents approximately 100 times too small to explain the observed field perturbations. A follow-up study (Smith & Achilleos, 2012) introduced a speculative feedback effect between auroral currents and electron precipitation as a driving mechanism for the asymmetric heat source. This produced currents of approximately the correct magnitude, but with three apparent flaws: (i) a temperature contrast of the order of 50K across the polar cap, (ii) a requirement for 5 MeV auroral electron energies, far in excess of observed values, (iii) a current distribution that was not m=1 symmetric (i.e. possessing a single line of symmetry), due to the feedback effect concentrating heating in a vortex-like wind structure. Nevertheless, this study demonstrated a possible mechanism for driving and sustaining wind systems that rotate at the planetary period in the thermosphere, with potential to explain the observations if the underlying assumptions of the model – for example the conductivity distribution – turned out to be flawed.

Subsequently, Smith (2014) argued that these thermospheric models were not plausible as explanations for the planetary period currents. This was for two reasons – first due to the large amount of Joule heating predicted to be associated with the required currents, and second due to the difficulty of sustaining a corotating temperature anomaly in a sub-corotating and highly sheared thermospheric flow (i.e. the thermosphere con-

tains closely located flows in opposing directions, resulting in significant shearing within the atmosphere). The first objection could be overcome if thermal energy was transported away from the polar regions more efficiently than believed at the time, for which there is now some evidence (Müller-Wodarg et al., 2019; Brown et al., 2020; Koskinen et al., 2021). The second is overcome if the feedback effect of enhanced electron precipitation driving the asymmetric heat source (Smith & Achilleos, 2012) – or something similar – was operational, since this provides a mechanism for generating and sustaining a structure within a sheared flow. In the absence of these processes, Smith (2014) proposed that it was more plausible for the planetary period current systems to be generated deeper in the atmosphere, in the Hall conducting layer. A series of papers (Smith et al., 2016; Smith, 2019, 2021) developed the Hall conductivity model further, demonstrating how Rossby waves in the upper stratosphere could potentially drive the planetary period currents. The main unresolved problem with these models is the ultimate location of the energy source driving the waves, which could be in the deep atmosphere, in the conducting layer, or in the magnetosphere. The lack of robust measurements of the Hall conductance in the polar regions also makes these models difficult to evaluate.

To begin to resolve exactly how Saturn's planetary period currents are generated, we need to understand the energy processes within Saturn's upper atmosphere, but as highlighted above, we have little detail on this. The only published past measurement to provide any temperature constraint within the planetary period phase was O'Donoghue et al. (2016), which showed a weakly constrained 50 K enhancement at planetary period phases between 45-90 $^{\circ}\Psi_N$. Chowdhury (2022) also constrained temperatures within a thesis chapter, using the same observations used within their velocity measurements. These also tentatively identified an average 50 K enhancement in temperatures around 90 $^{\circ}\Psi_N$, compared with 270 $^{\circ}\Psi_N$, with localized regions of temperature varying between 450 K and 350 K respectively, but these were associated with errors comparable with the temperature differences observed. Until recently, this was as far as our investigations could progress. Saturn's aurora was just too weak to be observed in detail, Cassini could no longer provide us with a planetary period current phase and so we had no way to better constrain Saturn's upper atmospheric induction processes.

Here, we utilize the first observations of Saturn's auroral H_3^+ made by the James Webb Space Telescope (JWST), to step beyond the past limitations of both ground- and space-based instrumentation, and observe Saturn's auroral energy distribution for the first time.

These observations were first examined in the companion paper to this (Stallard et al., 2025), hereafter described as Paper 1. In that study, broader regions of emission and background were summed and subtracted, to produce overall brightness maps for both the ionosphere and underlying layers. Herein, we take these same data cubes, and instead fit the emission spectrally, to extract details of the H_3^+ physical parameters, allowing the first spatially resolved maps of Saturn's H_3^+ ionospheric temperature, column density and total emission.

2 Data analysis

The JWST Near Infrared Spectrograph integral field unit (NIRSpec IFU; Jakobsen et al., 2022) observed Saturn's northern auroral region continuously through a Saturnian day, between 04:00-13:58 UT on 29 November 2024. At that time, Saturn was in late northern summer, approaching equinox in May 2025, providing us with a clear view of the northern pole. Our aim with these measurements was specifically to track and understand temperature changes within Saturn's auroral region, and so a 4-point ∼1.6 arcsec dither (a series of small positional offsets) provided an effective coverage of 5x5 arcsec per set of 4 individual observations. Using the F290LP/G395H filter/grating allowed us to observe numerous H_3^+ emission lines between 2.86-5.27 micron at a spectral resolution of R≈2700.

The data was pipeline processed and cleaned using the methodology outlined in Paper 1, but unlike that paper, which combined a range of wavelengths to produce pseudo-image-filters, we here will process the data to allow us to remove non-ionospheric background emission from data, before extracting and fitting the pure H_3^+ emission signal. Using this, we will construct a planetocentric spectral data cube of Saturn with a map scale of 0.5 degrees in the latitude and longitude directions (approximately 500 km in latitude and 150 km in longitude at the northern aurora). From this, we will then produce maps of the H_3^+ temperature and density across the auroral region.

2.1 Spectral background subtraction and fitting

Figure 2 shows the background correction and fitting process, tuned to the changing background at different planetary positions, for three different regions of the atmosphere, all at a longitude of 270°W (all latitude and longitude positions within this paper are in System III West kroniographic coordinates). The first column (blue) shows a spectrum at 80°N, inside the main auroral region, in a location where the reflected sunlight and thermal emission are relatively weak. The second column (green) shows a spectrum at 70°N, in a transition region away from the aurora, with increasing background signal. The third column (red) is within the sub-auroral region where dark spots of emission have been observed; here, H_3^+ emission is weaker, and the background signal is significantly stronger across all wavelengths.

For each column, we show the same background correction process:

0. Before being mapped into a spectral cube, data are partially passed through the JWST reduction pipeline (Bushouse et al., 2025). The reduced spectral data are contained within a 39x35 pixel data cube for each of the individual 104 images (notable for its difference in size from the original 30x30 pixel IFU, due to JWST pipeline processing). Spectral radiance is converted from MJy/sr to W/m^2/μm/sr. Because those pixels close to the limb cover very large regions of the map, we exclude pixels whose center is closer than 500 km to the 1 bar limb. Data from the top four and bottom three rows and the outer most columns of each data cube, along with any other data with NaN values, are also excluded due to data issues in these regions. From the remaining spatial positions within each data cube, we then calculate and scale the proportion of each latitude-longitude bin filled by that pixel (see Supplementary Figure 1 for clarification of this), to construct a planetocentric spectral data cube of Saturn with a map scale of 0.5 degrees in the latitude and longitude directions, with each of these positional bins containing a full wavelength spectrum.

   - We note here that, in combining measurements across a full planetary rotation, each longitude position consists of overlain data from a range of dayside local times, effectively smoothing out local time effects. Within the map, latitudes poleward of ∼60°N have at least 10 separate dithers contributing to them, and within the main auroral region (∼75°) more than 20 individual dithers contribute to the map (see Supplementary Figure S2a). This means that, between 8-16 UT, the largest gap in UT within each bin of the map within the main auroral region is, on average, 73 minutes (see Figure S2b). A future study will investigate Saturn's auroral variability in local time.

I. The first spectral row in Fig. 2 shows the raw spectrum across the entire 2.8-5.2 micron range at three positions of this data cube, at 80°N, 70°N and 60°N latitude, with all three positioned at 270°W longitude. From this full wavelength range, six sub-regions are chosen (because they contain both bright H_3^+ emission and background that can be modeled relatively easily), highlighted in gray. These regions are: 1) 3.270-3.470 microns, 2) 3.526-3.565 microns, 3) 3.610-3.630 microns, 4) 3.709-

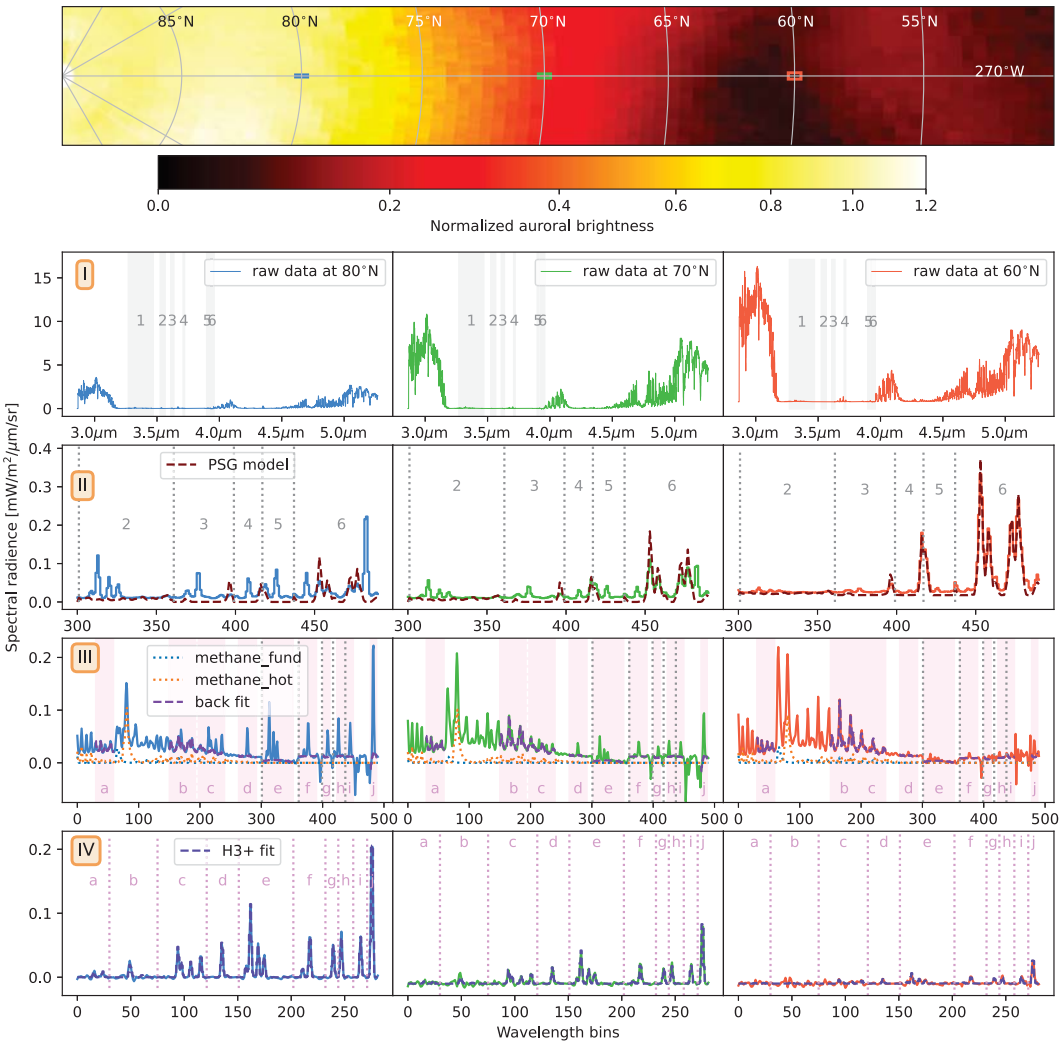

Figure 2. Spectral characteristics within Saturn's ionosphere. At the top, a thin slice of a polar plot of H_3^+ emission (taken from several wavelength ranges; see Paper 1) shows the reduction of H_3^+ emission brightness away from the main auroral region; here we show the normalized logarithm of H_3^+ brightness, to highlight weaker emission. On this, we note three latitude pixels (at 80°N in blue; 70°N in green and 60°N in red), all at the same longitude (270°W), with the spectra associated with these pixels shown in the three columns beneath (with matching blue, green and red line colors to correspond with the respective pixel positions these spectra are taken from). The top spectral row shows the pixel spectra after only limited pipeline reduction, with six sub-regions identified. The second spectral row shows five of these six regions, along with the scaled Planetary Spectral Generator (PSG) spectra for these regions (maroon dashed lines). The third spectral row shows all six of these regions, with PSG spectra subtracted. A second set of sub-regions is identified with a pink background, within which the fitted methane fluorescence and a background quadratic are also shown (purple dashed line). In the final spectral row, these secondary sub-spectra are shown with PSG, methane fluorescence and quadratic background all removed. To this, *h3ppy* fits the H_3^+ spectra (indigo dashed line). Most notable here is the relative strength of H_3^+ emission close to the pole, and the relative strength of background emission away from the pole; this contributes to a very strong gradient in ability to accurately fit H_3^+ emission away from the polar auroral region.

3.721 microns, 5) 3.890-3.911 microns, and 6) 3.923-3.958 microns. These sub-regions are then analyzed:

II. In the second spectral row in Fig. 2, the first background correction is applied to the previously defined sub-set of wavelengths. Here, sub-regions 2-6 contain varying amounts of reflected sunlight and internal thermal emission. To start to remove this background, the predicted spectral signature is modeled using Saturn's default settings within the Planetary Spectral Generator (PSG; Villanueva, Smith, Protopapa, Faggi, & Mandell, 2018; we note that the default output from PSG contains neither methane fluorescence nor H_3^+). For each sub-region separately, the top quartile of the PSG model spectrum (shown as a dashed dark red line) brightness is scaled to the top quartile of non-H_3^+ spectral brightness. This scaled PSG model is then removed from the spectrum. Sub-region 1 does not contain significant sunlight or thermal emission, but does contain significant methane fluorescence, corrected separately in the next step:

III. In the third spectral row in Fig. 2, we then apply a second background correction, like that used in past JWST temperature fitting (for example at Neptune; Melin, Moore, et al., 2025). Within the 3.0-3.6 micron wavelength region, the methane fluorescence is fitted with a combination of methane fundamental and hot band components.

- It is worth noting that methane fluorescence has significant non-LTE components, and this fit is not intended to be used to understand the complexities of methane fluorescence, but instead to remove it within a chosen wavelength range where the fit produces acceptable results. We do, however, show the result of the fit to methane hot band components later in the paper.

In addition to methane fluorescence, this background fitting also provides a quadratic polynomial fit to the remaining background, which accounts for sunlight in the 3.0-3.6 micron range, and also helps improve the background fit in other regions. Here, we have slightly modified the accepted wavelengths where this fit is applied in Melin, Moore, et al. (2025), removing some previously used regions due to corruption from Saturn's non-methane sources. The second narrower set of sub-regions each of these corrections is applied to is: a) 3.29-3.31 microns, b) 3.37-3.4 microns, c) 3.4-3.43 microns, d) 3.445-3.465 microns, e) 3.526-3.56 microns, f) 3.60-3.63 microns, g) 3.7105-3.718 microns, h) 3.8762-3.893 microns, i) 3.924-3.9318 microns and j) 3.9495-3.957 microns. These final wavelength ranges can then be fitted for temperature-dependent H_3^+ emission lines using the open source code *h3ppy* (Melin, 2025):

IV. In the fourth and final row of Fig. 2, we show the fully background cleaned spectrum. Each sub-region is taken from the wavelength range indicated in step III and, as a result, these regions cover a smaller number of wavelength bins, and the x-axis is reduced in size. This emission is fitted in two steps. Firstly, a ratio of the summed emission from the H_3^+ R lines contained in region (e) and the H_3^+ Q line contained in region (j) is measured. Using *h3ppy*, we have pre-calculated the modeled *h3ppy* relative brightness of these two regions over a range of temperatures, then fitted the change in this ratio with temperature with a second-order polynomial (as shown in the Supplementary Figure S3). As a result, using this pre-fitted quadratic, the ratio of the two regions provides a preliminary temperature T_{pre}:

$$T_{pre} = 198.6 + 227.16 \times \left(\frac{\sum R}{\sum Q}\right) + 37.285 \times \left(\frac{\sum R}{\sum Q}\right)^2 \quad (1)$$

This pre-fit is needed, as *h3ppy* tends to be highly sensitive to the pre-selected temperature, often failing if the initial temperature is too high or low. This pre-temperature typically results in a difference with the final fitted temperature of <50 K. Once the pre-temperature is calculated, *h3ppy* happily fits the full spectrum, first by guessing the density, then fitting across temperature, density, spectral resolution,

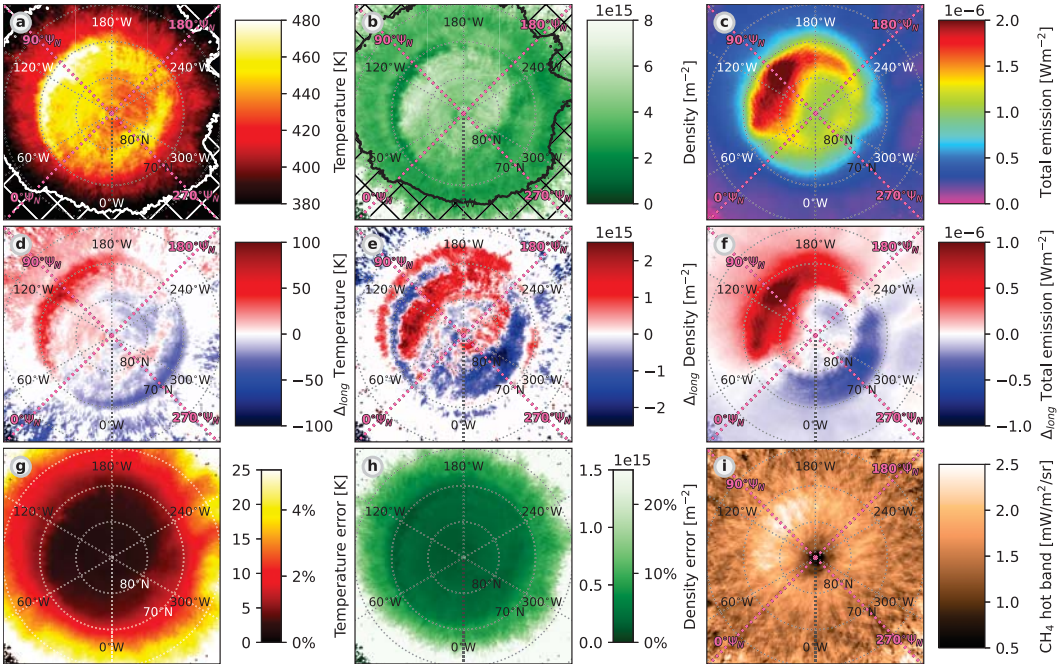

Figure 3. Saturn's northern auroral physical parameters. All panels show polar plots of the physical parameters in Saturn's northern auroral ionosphere. Panels (a) and (b) show a hatched region where the fitted error values are >5% and >1/3 respectively. Panel (a) shows H_3^+ ionospheric temperature, (b) shows H_3^+ column density and (c) shows H_3^+ total emission. The second row shows the same values as the top row, but here, for each latitude, the longitudinal median at that latitude has been removed, resulting in a difference values for each, (d) H_3^+ temperature difference, (e) H_3^+ density difference, (f) H_3^+ total emission difference (all three red positive, blue negative). In the bottom row, we show the calculated errors in fitting for temperature (g) and density (h) from *h3ppy*, as well as an estimated percentage error, compared with the highest temperature and density plotted in panels (a) and (b). The final panel (i) shows the modeled methane fluorescent hot band emission, used in cleaning the H_3^+ spectra, as in final two rows of Fig. 2. Panels (b), (c), (e), (f) and (h) show line-of-sight corrected values.

and Doppler shift. This fit also produces uncertainties for both temperature and density. From this fit, it is possible to calculate the total H_3^+ emission (Miller et al., 2013), a value which represents radiative atmospheric energy loss due to H_3^+, first introduced in Lam et al. (1997).

2.2 Line-of-sight correction

Once values are fitted, we can also apply a line-of-sight correction to convert the column density and total emission values from an emission angle column into a vertical column looking down on the surface of the planet from above, comparable to the correction previously applied at Jupiter (Stallard et al., 2018). Here, we assume a uniform shell of H_3^+ emission between 900-1300 km (based upon Stallard, Melin, Miller, Badman, et al. (2012)'s past auroral measurements of Saturn's auroral atmospheric column).

3 Results

In Figure 3, we show the results of this fitting process. The level of detail observed here represents a spectacular improvement from past observations, rivaling the highest-quality pre-JWST measurements of physical parameters in Jupiter's auroral region. The temperature map in Figure 3a shows a strong asymmetry in temperature, hottest in the sub-auroral regions at 120°W, and coldest around 300°W. Inside of this, filamented temperature structure is seen across the auroral region, with strands of heating and cooling at far higher detail than previous observations of Saturn, or even the highest resolution ground-based observations of Jupiter (e.g. Johnson et al., 2018).

The density map in Figure 3b reveals broad enhancement in the densities within the pole, particularly enhanced close to 75°N around 120°W, surrounded by a very low density arc at 71°N around 120°W. The polar region (at latitudes >80°N) have moderate enhancements in density. The main auroral emission fades in density both eastward and westward of 120°W, reaching a minimum at 300°W, slightly less dense than more equatorial regions.

When temperatures and densities are combined to produce a calculation of the total emission from all lines of H_3^+, shown in Figure 3c, this results in a very asymmetric aurora, brightest at 75°N that is also highly asymmetric, strongest around 130°W, with weaker polar emission across the polar region north of ∼80°N. Notably, the latitude of total emission aligns with the latitude of peak density, but the longitudinal emission peak aligns with enhanced temperatures. This highlights the shared contribution of temperature and density to the total emission, and why H_3^+ brightness might be misaligned with the phase of planetary period oscillations (e.g. Badman et al., 2012), skewed by thermospheric temperatures.

As previously discussed in Paper 1, this auroral enhancement close to 130°W is strongly indicative of an auroral region dominated by atmospheric planetary period currents rather than magnetospheric sub-corotation currents, since sub-corotation enhancements would not sustain an enhanced emission at a specific planetary phase, smearing out as the planet rotated. When observed in sequence, as in Paper 1, the enhancement is clearly observed as a bright spot that rotates with the planet. Both magnetospheric observations (e.g. Hunt et al., 2015) and observations of the southern auroral region by VIMS (Badman et al., 2012) show a strong auroral enhancement in phase with the planetary period current.

In order to compare our observations with past studies, it is useful to estimate a planetary period phase for the current system, since the phase from Cassini has been long since lost, based upon the variation in rotation rate observed in 2017 (Provan, Lamy, et al., 2019). The best measure of planetary period current system phase are the phases from the magnetospheric planetary-period oscillations, as defined in Hunt et al. (2014). From magnetic field measurements, the northern planetary period is defined by a peak upward current at $90°\Psi_N$ and a peak downward current at $270°\Psi_N$, reaching a minimal current at $0°\Psi_N$ and $180°\Psi_N$. Paper 1 used the auroral intensity as a guide to the northern planetary period phase Ψ_N, since upward currents close to $90°\Psi_N$ will produce enhanced auroral emission. However, historically, peak auroral brightness has both led and followed planetary period phase by tens of degrees (Badman et al., 2012; Bader et al., 2018).

For H_3^+ emission, this is partly a result of the influence of temperatures on the emission brightness. Instead, H_3^+ density can provide a more exact measure of the planetary period phase. This is because H_3^+ lifetimes are typically short in gas giant auroral regions: at Jupiter, they are no longer than 10 minutes across the entire polar region (Stallard et al., 2016), with half-lifetimes as short as two minutes in the auroral region (Nichols et al., 2025) and one minute on the Io spot (Mura et al., 2025), with later showing sig-

nificant reductions in lifetime for the brightest emission. Equally, Saturn's infrared auroral brightness is dominated by electron precipitation (Badman et al., 2012). Particle precipitation processes are not always driven by currents, most notably at Jupiter, where broad band precipitation contributes more than 90% of the total precipitating particles (Salveter et al., 2022). However, despite this, Jupiter's auroral power is strongly correlated to magnetospheric currents (Nichols & Cowley, 2022), suggesting that the majority of auroral broad band precipitation is produced by instabilities that are associated with auroral currents (Mauk et al., 2017). As such, the observed auroral column densities provide a good proxy for changing particle precipitation flux, with higher densities indicating stronger upward currents and lower densities indicating weaker upwards or downwards currents, assuming that it is the northern phase that dominates Saturn's northern ionosphere and atmosphere, as indicated by Chowdhury (2022).

As a result, here, we use changing H_3^+ column density to estimate the planetary period phase. Given the complex sequence of reversing density peaks and dips we observe, we align our observations using the region where the planetary period current is weakest, at the balance point between upward and downward currents. Measuring the location where the H_3^+ column density most closely matches the median value (the values closest to zero in Fig. 3e), this axis of symmetry in the density measurements can aligned with the minimum currents at $0°\Psi_N$ and $180°\Psi_N$. This results in a slightly revised phase of $0°\Psi_N$ at 45°W (rather than 55°W in Paper 1).

The observed auroral asymmetries, in phase with the planetary period, are revealed even more strongly by subtracting the median values across all longitudes, individually measured in each bin of latitude, shown for temperature, line-of-sight corrected density and total emission in panels d), e) and f) respectively. Here, the main constraint is the relatively weak sub-auroral differences observed when compared with the errors in our fitting. For both temperature d) and column density e), we have set the difference values to zero anywhere the difference from median values are less than the fitted errors.

All three parameters are dominated by planetary period phase across all latitudes where these values are significant. Temperatures (Fig. 3d) are clearly hottest (480 K) at the region equatorward of the main auroral region (between latitudes of 70−73°N) near $90°\Psi_N$ and coldest (400 K) in direct anti-phase with this, again just equatorward of the main aurora (between latitudes of $70 - 73$°N) near $180°\Psi_N$. This temperature gradient is ∼150 K across the entire auroral region. Inside the region of main emission, the temperatures are more moderated, varying across this region by only ∼50 K. This appears offset from previous observations by O'Donoghue et al. (2016), where the main temperature gradient was measured either side of $90°\Psi_N$, and broadly agrees with measurements by Chowdhury (2022) peaking at $90°\Psi_N$, though these were both poorly constrained within errors.

This heating and cooling in phase with the planetary period extends equatorward, with a broad region of $< \pm 25$ K heating and cooling on either side extending as far as is statistically meaningful, down to latitudes >55°N. The majority of the sub-auroral temperature is smoothly structured, but between $240 - 300$°W, it varies sharply at locations close to a region where dark ionospheric beads have previously been observed in Paper 1. The temperature structures in this region are at the edge of statistical separation above the fitting errors, but the largest dark bead, shown as a pinkish region between $260 - 290$°W and $60 - 65$°N in Fig. 3c, appears to align with a statistically significant cool region, between 350-370 K, ∼50 K lower than the median. The brighter regions are warmer than the beads (∼400 K), but we cannot statistically separate between cold spots surrounded by median temperatures, and a broad cool region with hot material between the beads.

In H_3^+ column density (Fig. 3e), the clearest signature is an asymmetry associated with the main auroral emission. There are three bands of anti-phase auroral emission,

all strongly aligned with planetary phase. At 90°Ψ_N, the H_3^+ density alternates between strong-weak-strong-weak (red-blue-red-blue) from two *sub-auroral*, the *main auroral* and *polar* regions (at latitudes between 67−70°N, 70−73°N, 73−81°N and 81°N and the pole, respectively). At 270°Ψ_N, the polar H_3^+ column density is in almost exact anti-phase with this, alternating between weak-strong-weak-strong (blue-red-blue-red) again between 67-70°N, 70−73°N, 73−81°N and 81°N and the pole, respectively - however, it is notable that the strength of this alternation appears much less statistically significant at 270°Ψ_N equatorward of 73°N, as values fall below the error limit (likely due to the reduced temperatures in this region). The strongest contrast is seen between the main auroral region and its surrounding sub-auroral region, with smooth weak emission differences seen equatorward of this and weakest in the polar region. The values measured, ranging between 2-8 $\times 10^{15}$ m^{-2}, match well with the minimum values measured by O'Donoghue et al. (2016) in previous ground-based observations, but are smaller than the highest values previously observed, which measured values as high as $\sim 2 \times 10^{16}$ m^{-2} near 90°Ψ_N.

In H_3^+ total emission, these subtle differences are lost, instead resolving out as a clear brightness asymmetry, brightest at 90°Ψ_N and weakest near 270°Ψ_N. This strongly correlates with the asymmetries previously observed in H_3^+ brightness in Paper 1, along with the weak sub-auroral darkened beads detected in around ∼60°N and between 180−300°W. The auroral values measured, ranging between 0.5-2 $\times$ 10^{-6} Wm^{-2}, are much lower than those measured by O'Donoghue et al. (2016), who measured values between 6-10 $\times$ 10^{-6} m^{-2}.

Figure 3g and h both show that these observed variations are significantly larger, by a factor of 20 for temperatures and a factor of 5 for column density, than the measured errors for the auroral region. We do not show total emission errors. Nominally, these could be calculated by factoring the temperature and density errors with one another, but the resultant value would massively over-estimate the total emission errors, since the main contributor to fitting error is the anti-correlation between temperature and density (Melin et al., 2013), with total H_3^+ emission originally being devised specifically to provide a value not-effected by this anti-correlation (Lam et al., 1997). Errors will exist, but are hard to calculate directly, requiring an empirically modeled test of variations for a given noise level.

Notably, significant regions of the pole show direct correlations between the temperature and density (i.e. Figs 3d and e are both red, or both blue), in particular the broad scale structures within the auroral region. Such correlation is surprising, since these values are more typically anti-correlated (Melin et al., 2013). This anti-correlation is the result of one of two processes within auroral regions: (1) higher H_3^+ density drives enhanced cooling, reducing the H_3^+ temperatures, or; (2) higher H_3^+ density is an indicator of enhanced precipitation flux, which is often coupled to higher particle precipitation energies, driving the H_3^+ peak deeper, into colder thermospheric altitudes. It is also possible that changes in H_3^+ density are driven by interactions between H_3^+ and the surrounding ionosphere, since changes in electron density produce changes in the H_3^+ destruction rate, as previously observed at Saturn within the regions coupling to Saturn's rings (O'Donoghue et al., 2013; Moore et al., 2015).

These direct correlations show that the temperature structures are indicators of localized heating, rather than an artifact of changing precipitation depth or changing cooling rates. However, it is possible that the strongest enhancement in temperature, close to 70 − 73°N and 90°Ψ_N, could be the result of weaker precipitation, associated with the very weak column densities in this region. In the polar region, temperatures on the 90°Ψ_N side of the 0 − 180°Ψ_N line are highly correlated with column density, but on the 270°Ψ_N side they are also anti-correlated, again potentially being driven by changing precipitation depth, changes in in-situ cooling or interactions between H_3^+ and the surrounding electrons.

Finally, Figure 3i shows the fitted hot band methane fluorescence modeled in step 3 of the data fitting process. While this does not give an accurate measure of the true methane fluorescence, since that emission is highly non-thermal and requires detailed modeling to fully understand, it does give a broad overview of the changing emission brightness of fluorescing methane hot bands within the auroral region. Paper 1 showed no auroral enhancement within fluorescing fundamental methane emissions, suggesting that only the methane hot band emission is aurorally enhanced.

4 Discussion

Firstly, let us caveat these observations. This is a single (∼10 hour) day of observation, and the extent of planetary period control over the auroral region may change on other days, and during periods of solar-wind associated activity, it will almost certainly be more strongly controlled by local-time dominated auroral processes.

However, during this Saturnian day, the entire auroral region provides a unique picture of the ionospheric interactions through a full planetary rotation, relatively free of local time dependency, combining dithers from a wide range of local times, with a maximum gap between local times of just ∼73 minutes. Saturn's aurora is often highly variable as a result of magnetospheric interactions; but such dynamics would be asymmetrically smeared through the planetary rotation. As a result, this data provides a unique new window into the dynamics involved in a single rotation, one strongly dominated by variations associated with the planetary period current.

4.1 Saturn's ionosphere mapped into the planetary phase

The delicate changes observed in both temperature and density structure are far more sensitive than any past measurements, providing us with a unique view of the changing auroral conditions through a full rotation. The incredible reflection and inversion of both temperature and density features within Saturn's ionosphere reveals the dominance of the planetary period currents during this period. This is particularly notable where the temperature and density are correlated.

However, this approximate alignment between the temperature and column density enhancements, both peaking near a planetary period phase of $90°\Psi_N$, is somewhat challenging when compared with past theory of how planetary period currents are generated. Both theoretically require both a perpendicular flow between the neutral twin-cell vortex that powers the currents and the Pedersen currents flowing through the ionosphere, and a direct alignment between the source of heating and the flow of that heat out across the auroral region; the atmosphere flows radially away from a localized heat source, thus driving $\mathbf{E}\times\mathbf{B}$ forces that drive perpendicular winds, as described from the magnetospheric perspective in Jia et al. (2012) and from the atmospheric perspective in Smith (2014).

The Smith (2011) model takes a different atmospherically-focused approach, enforcing a thermospheric heating that then drives neutrals and ions, resulting in current divergencies that can drive planetary period currents out into the surrounding magnetosphere. A direct comparison between our data and this model can potentially better highlight the origin of the planetary period currents.

4.2 Direct comparison with ion winds and atmospheric modeling

In Figure 4 we directly compare our temperature and column density measurements with past Keck measurements of the ionospheric twin-cell vortex observed by Chowdhury et al. (2022), and the temperature and current divergency modeled in Smith (2011), as well as the horizontal neutral winds and currents produced by that model.

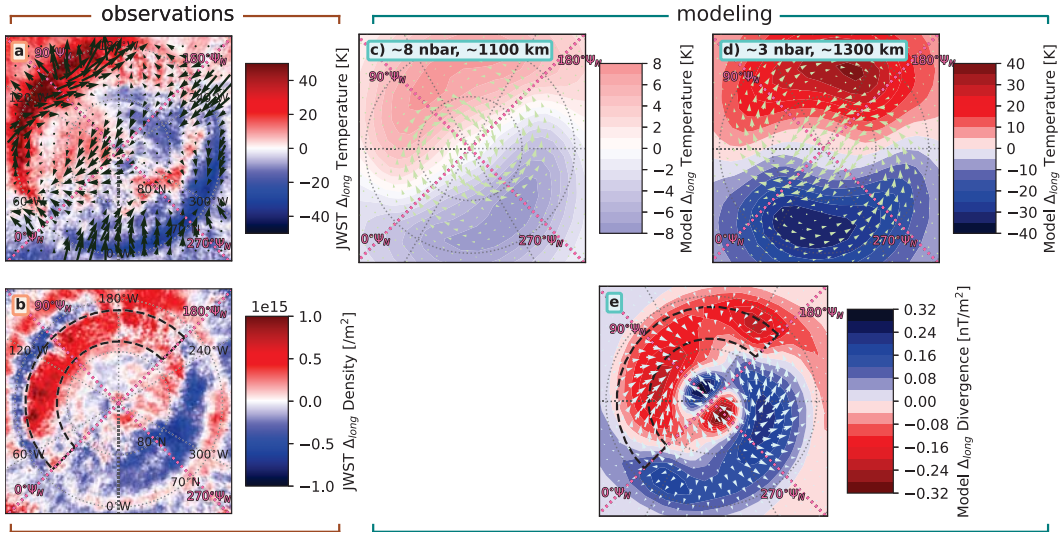

Figure 4. Comparisons between the temperature and density differences observed by JWST, and comparable values from Smith (2011). Here, the left panels are our observed values of difference in temperature (top; as Fig. 3d) and column density (bottom; as Fig. 3e). On the top left, we have replotted the vector ion winds observed by (Chowdhury et al., 2022) using the Keck telescope, rotated so that $0°\Psi_N$ aligns with 45°W. To the right of this, we show outputs from Smith (2011)'s model, rotated so that the integrated current divergence (bottom right) best matches with our observed column density. The top right two panels each show filled contours of the modeled temperature difference at pressure level n=6 (middle; shown in Smith, 2011 as Fig. 4) and pressure level n=8 of the model, along with the modeled thermospheric horizontal neutral wind velocities (pale green arrows, with the longest arrow representing ∼20 m/s and ∼30 m/s respectively). In the bottom right panel, we show contours of the height-integrated electric current divergence, showing regions of upward (negative divergence; red) currents and downward (positive divergence; blue) currents. The integrated horizontal currents are shown (pale blue arrows, with the longest arrow representing a current of ∼1 mA/m). In both bottom panels, we also show the location where Smith (2011) positioned the heat source driving these differences (black dashed box).

Aligning the past observations of ionospheric winds with our dataset is relatively simple, since the Doppler shift measurements made by Chowdhury et al. (2022) were specifically grounded to planetary period phase by simultaneous measurements from the Cassini spacecraft. As a result, we can simply rotate the twin-cell vector field observed by Chowdhury et al. (2022) to match with our 45°W at $0°\Psi_N$. The comparison between these datasets in the top left panel of Fig. 4, appears to show some beautiful alignments, despite the seven year gap between their observations. Though Chowdhury et al. (2022) clearly observed a poleward flow towards $0°\Psi_N$, the flows along the flank near $90°\Psi_N$ appeared to split. Here, we see that this split in ion flows is likely driven by neutral winds flowing directly out from the region of highest heating. Between $260-350°\Psi_N$ ions appear to be drawn into the pole across the region of cooling.

The region of highest temperatures, between 100−160°W and 70−73°N, is particularly noteworthy, since the co-located column densities in this region are very low, in fact lower than any other measured part of the ionosphere within JWST's field of view, including much more equatorial regions. As such, the measured H_3^+ density is unlikely to simply be the result of reduced particle precipitation, which at most would reduce the H_3^+ density back to the background solar ionization level. It instead suggests one of two drivers. One possibility is that the region of high temperature is produced by a very high flux but low energy particle precipitation. Past modeling of soft electron precipitation has shown that it can produce large amounts of secondary electrons that increase dramatically in temperature (Galand et al., 2011). Enhanced electron densities in this region could then potentially destroy H_3^+, lowering the H_3^+ density below the EUV background values. Alternatively, the ion flows observed by Chowdhury et al. (2022), flowing away from this hot region in all directions, may be actively excavating H_3^+ from this region, leaving it as an anomalously low density region.

Before we can directly compare our data with the Smith (2011) model, we have to align the data with the model. Since Smith (2011) directly modeled the generation of these currents from thermal flows, and was written before a planetary phase was defined by Hunt et al. (2014), we need to align the model outputs into a planetary period phase. As described above, we estimated a northern planetary period phase using the regions where the H_3^+ column density approaches the median value at 75°N as a proxy for the planetary phase line between $0°\Psi_N$ and $180°\Psi_N$.

We can apply a similar principle to the current divergence values in Smith (2011), aligning $0-180°\Psi_N$ phase line with the median values in current divergence again within the main auroral region, with enhanced currents falling in the $90°\Psi_N$ sector between these values, and reduced currents falling in the $270°\Psi_N$ sector. In doing so, we can compare the model with our data, as well as with the wider literature that uses planetary phase as a constraint.

Having assigned a planetary period phase to the structures within the Smith (2011) model, we reveal three important qualifiers that potentially address the expectations from magnetospheric models (shown in Fig. 1); that closing currents should flow perpendicular to the $0-180°\Psi_N$ line (from $270°\Psi_N$ to $90°\Psi_N$), and atmospheric neutrals should flow parallel to the $0 - 180°\Psi_N$ line from $180°\Psi_N$ to $0°\Psi_N$. We compare these modeled values with observations in Figure 4:

1. A simple expectation of neutral flows might be that they would flow from hot to cold over the pole, from the hottest regions at $90°\Psi_N$ to the coldest at $270°\Psi_N$. Instead, flows are twisted westward by the sub-rotating polar cap, so that the transpolar neutral flows are offset from the $90-270°\Psi_N$ line by ∼45°W at ∼1,100km (Fig. 4c), flowing over the pole from $\sim135°\Psi_N$ to $315°\Psi_N$, before twisting further at ∼1,300km (Fig. 4d), flowing over the pole from $\sim175°\Psi_N$ to $355°\Psi_N$. As a result, neutral winds actually do flow from broadly from $180°\Psi_N$ to $0°\Psi_N$, as shown

in many papers (e.g. Smith, 2014; Hunt et al., 2014; and in Fig. 1), and observed in ion winds by Chowdhury et al. (2022).

2. However, while these neutral winds produce in a strong negative divergence (upward current) around 90°Ψ_N and positive divergence (downward current) around 270°Ψ_N, the direction of altitudinal-integrated horizontal currents over the pole are complex (Fig. 4e). These twist significantly around the region of highest divergence, but approximately flow over the pole from ∼300°Ψ_N to 120 °Ψ_N. Since the horizontal currents are integrated across all altitudes, they are twisted from polar neutral winds at specific altitudes, offset closer to 130−170° longitude with those winds closest to expectations at 1300 km (Fig. 4d).
3. The source of heating (effectively positioned on the 90°Ψ_N side of the planet, between 0−180°Ψ_N) in the atmosphere is offset from the location of enhanced temperatures, with atmospheric dynamics moving heat away westward from the region of heating, only around 10° at 1100 km (Fig. 4c), but closer to 45° westward at 1300 km where temperatures are higher (Fig. 4d). Notably, the model's heat source (the dashed half torus in Fig. 4e), aligns more closely with the region of negative divergence than the overall temperature structure.

The overall shape of current divergence (Fig. 4e) modeled by Smith (2011) matches with our observed column densities (Fig. 4b) surprisingly well. While negative divergencies (associated with upward currents and thus the downwardly-accelerated electrons that drive aurorae, red in Fig. 4e) are spread across almost all planetary phases, they are most strongly negative at phases between 30−120°Ψ_N, where our column densities are highest. This matches the leading statistical H_3^+ auroral brightness measured in Cassini-VIMS (Badman et al., 2012), peaking between $0 - 90°\Psi_N$, but contrasts with the statistical lagging UV emission brightness, peaking at around ∼115°Ψ_N (Bader et al., 2018). The strongest positive divergence (blue in Fig. 4e, associated with downward currents which weaken upward co-rotation currents and thus also weaken the associated downwardly-accelerated electrons that drive aurorae) occurs between 190−280°Ψ_N, again aligning with the region of lowest column density.

It is worth noting that while the polar regions are twisted by the magnetospheric torque, the equatorial regions are expected to be uniform. The significant heating we observe down to at least 55°N is highest at 90 °Ψ_N, and might be expected to drive neutral (and weaker ion) flows both East and West towards the cooler regions around 270 °Ψ_N. This could explain the twisting in the planetary period phase observed within magnetometer data taken near Saturn's rings (Provan, Cowley, Bradley, et al., 2019), where the peak planetary period oscillations were observed close to 0 °Ψ_N instead of 90 °Ψ_N. However, a neutral wind flowing East at 0 °Ψ_N and West at 180 °Ψ_N would be expected to drive Pedersen currents towards the equator and towards the pole respectively, in the wrong direction - this would be expected to have the strongest upward current at 180 °Ψ_N. Clearly, the processes that drive current closer within Saturn's equatorial regions are complex.

More compelling is the reversal of both current divergence and column density difference within the polar region. These appear to be in direct anti-phase with the values on the main auroral region suggesting pairs of upward and downward currents flowing between the main auroral regions and the poles. The locations of these are incredibly well-aligned, switching in both divergence and column density difference at a latitude of 82°N and peaking at a latitude of 87°N and a planetary phase of 90 and 270°Ψ_N. Upward and downward currents poleward of 80°N will largely be on open field lines, and so are ignored in magnetospherically-focused diagrams models of the planetary period currents (e.g. Hunt et al., 2014), but magnetometer measurements of this region also identify this reversal in their data between $80 - 85$°N (see Figure 7 of Hunt et al., 2015).

One contrast between Smith (2011) and our observations is the strong weakening in the H_3^+ density (Fig. 4b) equatorward of the main emission, compared with only a very weak modeled positive current divergence (Fig. 4e). As discussed above, the very low column densities here may be the result of enhanced destruction or removal processes, but there is notably a matching localized enhancement in density on the 270°Ψ_N side of the oval at similar latitudes, along with a comparable reversal of the current divergence to more negative in a similar location. While models of the planetary period current do expect an equatorward reversal, this is typically expected away from the auroral region, and no reversal is observed in currents equatorward of the main auroral emission (Hunt et al., 2015). Equally, Smith (2011) does not model the apparent third reversal at even more equatorward regions. This might indicate that JWST has revealed an even more twisted spiral of heating and cooling away from the auroral region than is captured by Smith (2011), perhaps similar in structure to the spiraling temperatures modeled as a result of local time heating within Saturn's thermosphere, that extend down to the equator (Iñurrigarro et al., 2024).

Having aligned our data to the Smith (2011) model, temperatures can also be directly compared. Pressure level = 6 is the model layer with largest Pedersen currents and, at a median altitude of ∼1,100 km, is the layer most aligned with Saturn's observed emission peak (Stallard, Melin, Miller, Badman, et al., 2012). At this level (Fig. 4c), there is a notable difference in magnitude between the observations and model, with Smith (2011) only producing temperature differences of $\sim \pm 8$ K, though this also greatly underestimated the required currents and more recently observed ion winds associated with this current system (Chowdhury et al., 2022). The temperatures observed are closer in scale to those in the Smith and Achilleos (2012) model, though those are a specialized case where asymmetries in temperature structures drive a varying rotation rate, unlike the symmetry observed here. The observed temperatures (380-450 K) are much lower than those required by Smith (2014), requiring Jupiter-like temperatures between 700-1000 K. However, while the absolute value of the Smith (2011) model's temperature gradients and neutral winds are much lower, we do see surprisingly similar morphology at 1100 km. Temperatures are spread out equatorward of the main auroral emission, though our measured temperatures seem to increase more in the sub-auroral region compared with the model, and our observed temperatures appear more balanced either side of 90 and 270°Ψ_N. The flows observed do approximate to the flow directions observed by Chowdhury et al. (2022), but are mis-aligned by about 45°E.

At pressure level = 8, positioned at ∼1,300 km (Fig. 4d), slightly above the observed H_3^+ emission peak, the temperature structure is similar in magnitude, but appears to be rotated westward, compared with our observed values. However, the modeled neutral wind flow vectors at this altitude match incredibly well in direction to the ion winds observed by Chowdhury et al. (2022), with the observed ions expected to be dragged with the neutral atmosphere. These co-aligned polar flows, both flowing from 180°Ψ_N to 0°Ψ_N before veering west at a similar latitude, as well as showing similar flow patterns on the inner edge of the return flow around 90°Ψ_N.

4.3 How to sustain an asymmetric heat source in the thermosphere

The observations support the basic assumptions and thermospheric modeling results of Smith (2011) in demonstrating that there is an asymmetric heat source in the thermosphere (i.e. the black dashed lines in the bottom panels of Fig. 4), and that it drives currents as predicted. The question is: are we witnessing the process that drives the planetary period currents, or another secondary effect driven by this system of currents?

If Saturn's thermosphere were the ultimate driving mechanism of these currents, perhaps via the feedback mechanism of Smith and Achilleos (2012), then the existing problem of how the north and south planetary period current systems became 'locked'

in 2013-2014 would be more difficult to resolve, since a mechanism for the feedback effects in the north and south to communicate with each other would need to be discovered.

It is possible, though, that the Pedersen currents implied by these observations are not the primary driver of planetary period currents, but exist alongside Hall currents driven from deeper layers of the atmosphere, and it is the Hall currents that dominate the observed planetary period current systems. This scenario was envisaged in the discussion section of Smith (2021) which proposed that the atmospheric waves in the stratosphere could potentially penetrate into the Pedersen conducting layer and drive small Pedersen currents which could transfer energy to and therefore drive the magnetosphere.

Past observations of the ultraviolet (UV) auroral emission are unclear about the depth of particle precipitation, with the measured altitudes from UV images placing the aurora between 800-1200 km altitude, yet measurements of hydrocarbon absorption of this auroral emission compared with models suggests a much lower altitude of >610 km (Gérard et al., 2009). Our measurement of the methane hot band fluorescence shown in Fig 3i, reveals emission from the upper stratosphere that includes a brightness enhancement that is very well correlated with our brightest emission. Notably, Paper 1 showed no comparable enhancement in the fundamental emission, while JWST observations of Jupiter have shown that the main emission at Jupiter has significantly stronger fluorescence enhancement in the methane hot band emission, compared with the fundamental emission (Melin, Stallard, et al., 2025). This suggests that there is a significant source of either heating or excitation of the methane within the fluorescence emission peak at ∼600 km altitude (Stallard, Melin, Miller, Badman, et al., 2012).

One indicator for the extent to which these currents are dominated by Pedersen or Hall currents is the temperature structures measured herein. The main source of thermal gradient observed in these observations results from a narrow band enhanced temperature difference at ∼70°N. This tightly confined region is well outside the primary region for direct particle precipitation heating, highlighted by enhanced column densities in Fig. 3e, suggesting the heat has moved away from the auroral source, as predicted by Smith (2011) and Smith and Achilleos (2012). However, this heat source is located in a region where the ionosphere is significantly sub-corotating (Stallard et al., 2004).

If Saturn's thermosphere is at all like Jupiter's (Wang et al., 2023), the neutral thermosphere in this region will also significantly sub-corotate. This would drag heat away from the planetary-phase, with the shearing winds redistributing the heat across all longitudes within a single rotation. However, these temperature differences could be sustained within the stratosphere if this sub-rotation fades between 600 and 1100 km. If these underlying temperature differences are deeply confined, heating the thermosphere through vertically propagating waves, as suggested by recent modeling (Smith, 2024), which would suggest deeper Hall currents dominate the overall planetary period currents, with the Pedersen current flows revealed in the upper ionosphere (Chowdhury, 2022), driven by the temperatures observed here, making only a partial contribution. The extent to which each contributes can only be ascertained through detailed modeling, that this dataset will uniquely allow.

One alternative source for the differential rotation rate is the equatorial thermosphere, rather than the deeper polar regions. The ∼100 K thermospheric temperature gradient we observe equatorward of 65°N (the mapped location of Enceladus, where the breakdown in corotation begins; Stallard, Melin, Cowley, Miller, & Lystrup, 2010) is well outside the direct ion drag driving of the outer magnetosphere. If this thermal gradient is sustained, it should allow heat to move at approximately the rotation rate of the planet, with a difference in thermospheric sub-corotational winds of only 100-200 m/s between the summer and winter hemisphere to match with observed magnetospheric rotation rates.

The feedback mechanism within Smith and Achilleos (2012) may not be enough, alone, to sustain the temperature differences observed here, or contained deeper within the atmosphere. However, both the northern and southern planetary period currents directly alter the thickness and locations of the current sheet within the surrounding magnetosphere (e.g. Morooka et al., 2009; Provan et al., 2012; Thomsen et al., 2017; Cowley & Provan, 2017; Agiwal, Hunt, Dougherty, Cowley, & Provan, 2020; Provan, Bradley, et al., 2021), with a thinning of the current sheet being strongly correlated with reconnection signatures in magnetic field data associated with both tailward propagating plasmoids and planetward propagating dipolarizations (Jackman et al., 2016; Bradley et al., 2018).

Recurrent dipolarizations have been observed to result from individually generated reconnection bursts occurring sequentially at similar favorable planetary period phases (Cowley & Provan, 2021), and overall, such reconnection events typically contribute about a fifth of the total mass loss from Saturn's magnetosphere, though at some advantageous times becoming the dominant mass loss process (Agiwal et al., 2022). Such reconnection events have been associated with localized enhancements in the auroral brightness (Bader et al., 2019). There is also a weak association between the phase of planetary period currents and plasma instability interchange events, further driving energy into the inner magnetosphere, producing auroral enhancements (Azari et al., 2019).

The planetary period phase was observed to change in dramatic jumps during periods of solar wind compression near equinox (Provan et al., 2015), with similar compressions often resulting in dramatic auroral enhancements (Clarke et al., 2009), with this auroral strengthening most likely driving more heat into the ionosphere as at Jupiter (Stallard et al., 2002; O'Donoghue et al., 2021). Hunt et al. (2020) showed that the relative latitudinal locations of both the upward planetary period currents and upward sub-corotation currents are maintained across local time, implying an intrinsic link between the two systems.

As such, while the planetary period currents are driven by the temperature structures revealed here, the temperature asymmetry alone, preferentially varying incoming middle magnetospheric currents, might not be enough to sustain the continuous heat flow that drives these currents. Instead, it may be both the continuous auroral enhancement and weakening on either side of the auroral oval associated with this steady auroral heating, combined with the pulsing of magnetospheric events caused by changes in the magnetosphere wrought by this current system that ultimately provide the feedback loop that sustains this auroral system. Given the alignment of the modeled heat source with the region of strongest upward currents, localized enhancements in the aurora from magnetospheric process would pulse heat into the planetary period current system exactly where it is needed to enhance these currents.

We note, however, contradictory to this, that Bader et al. (2018) show the highest overall UV emission when the northern and southern phases are in antiphase with one another, and yet, these same periods show the lowest variation with northern phase. This perhaps suggests the planetary period currents actually limit enhancements from the magnetosphere at the planetary phase where brightening occurs.

5 Conclusion

These observations of Saturn's auroral region represent a huge step forward in our understanding of Saturn's auroral ionosphere, as well as the currents associated with the planetary period current system. Past measurements of the auroral brightness within a single rotation have been challenging in the UV with Cassini and impossible with Hubble, due to the cadence of those orbits around Saturn and Earth respectively; Cassini-VIMS could produce weak measurements of individual planetary rotations (see supple-

mentary movie S1), but never at a sensitivity to be scientifically useful. We have compared the observations here with the statistical intensity of the aurora, but these measurements were made over many Saturnian days (e.g. Kinrade et al., 2018; Badman et al., 2012).

However, detailed spatially-resolved measurements of auroral H_3^+ temperatures and densities have never previously been possible. Previous statistical averages typically had errors of $\pm$50 K, on par with the largest temperature differences revealed here. With expectations for JWST's one-hundred-fold improvement in signal-to-noise over Keck, we hoped for a ten-fold improvement in our errors. Here, the ten-fold improvement is seen in each 0.5° latitude-longitude bin, resulting in incredible acuity, revealing delicate filamented temperature structures. Equally, column density details are revealed for the first time with incredibly low density errors, again with an up to ten-fold improvement, where our best past measurements have had ∼50% errors over much broader regions (e.g. O'Donoghue et al., 2016).

Saturn's ionosphere and aurora have been shown to be highly orientated in rotational phase, aligning with past expectations of an aurora dominated by the variations caused by the planetary period auroral current. From this, we assume a northern planetary period phase of $\sim 0° \Psi_N$ phase at 45°W at the time of these observations.

Temperatures range between 403-489 K (the central 98% quantile), with localized variations observed, across <10° regions, resulting from changes in temperature of only 20-30 K. Temperatures are strongly enhanced around a planetary period phase of $\sim 90° \Psi_N$, partially agreeing with the weakly constrained measurements from O'Donoghue et al. (2016) and Chowdhury (2022), but here revealing a matching cooling at $\sim 270° \Psi_N$, with the strongest heating/cooling at 70°N. There is also weaker heating/cooling in the sub-auroral region, which remains statistically significant as far equatorward as ∼55°N.

We have also identified statistically significant cooling focused on the darkest of the sub-auroral beads previously identified (Paper 1), between 240−300°W. While we cannot statistically resolve the density changes across this region, this does indicate the brightness differences are at least partially controlled by a thermospheric cooling within beads themselves, strengthening the case these are the result of atmospheric dynamics, either propagating from below or moving within this layer of the thermosphere. Further observations investigating these features is needed to understand how and why they are formed, and whether they are associated with the aurora, the observed underlying stratospheric complexity, or a combination of both.

Column density measurements suggest alternating bands of upward and downward currents, reflected and inverted either side of the $0-180° \Psi_N$ line. These measurements reveal more complex structures in the planetary period current system than have ever been seen before, but broadly agree with past spacecraft measurements (e.g. Hunt et al., 2015) and the predictions from modeling (e.g. Smith, 2011). Most notably, the main auroral emission is enhanced and reduced by comparable amounts through the rotating upward and downward currents, resulting in $\pm 2 \times 10^{15}$ m^{-2} density differences.

Notably, past models place the heating source, yielding temperature distributions similar to those observed here, directly over the region of highest column density, indicating that the aurora itself is the heat source for the planetary period current. Since the region of highest temperatures (around 70−73°N) is well away from the peak auroral region (around 75°N), at the region of the thermosphere that significantly sub-rotates at >1 km/s, we speculate the main heat sink within the atmosphere is found deeper in the atmosphere, beneath the region modeled by Smith (2011). This deeper upper stratospheric region (∼600km; Stallard, Masters, et al., 2012) has significant enhancement of the methane hot band fluorescence that most closely aligns with the H_3^+ total emission, suggesting this layer is equally affected by both temperature enhancements and incom-

ing precipitation. That suggests significant auroral energy is penetrating into this layer, driving similar localized heating, but resulting in potentially very different thermal winds.

According to Smith (2014), if the underlying layer is heated similarly to the thermosphere, producing a hot spot near $90°\Psi_N$ and a cold spot near $270°\Psi_N$, neutral winds would flow directly across the pole, dragging ions more slowly with them, but leaving electrons magnetized and stationary on magnetic field lines. This, combined with the localized enhancement in Hall conductivity within the auroral region, results in an effective $\mathbf{E}\times\mathbf{B}$ drift and Hall current flowing across the local auroral regions at $90°\Psi_N$ and $270°\Psi_N$, resulting in the same negative current divergence and upward currents at $90°\Psi_N$, and the same positive current divergence and downward currents at $90°\Psi_N$. From this, we predict that the planetary period Pedersen currents driven within the thermosphere make up only part of the entire current, with a significant additional contribution coming from deeper Hall currents. We speculate that the planetary period currents might be further enhanced by the changing magnetospheric conditions that result from these currents, driving a feedback loop of enhanced reconnection and precipitation in phase with the atmospheric current system.

This result has important implications for other planets. If the atmospheric conditions can drive currents out into the surrounding atmosphere, detailed measurements of the stratospheres of these worlds may help reveal more complex interactions, acting to enhance and weaken the aurora in unique and, as yet, unexpected ways.

Ultimately, we have revealed the temperature structures that appear to drive the planetary period currents, either within the thermosphere or deeper, and have associated these temperature structures with heating from the magnetosphere. Further modeling of the atmosphere, ionosphere and magnetosphere are needed to fully understand this complex system, but the temperatures presented here provide the unique and specific key, previously missing, that will allow these models to fully resolve the processes that produce Saturn's unique planetary period current.

Open Research Section

Raw data used in this publication is currently under embargo and so is not yet available from the Mikulski Archive for Space Telescopes (MAST). However, the partially processed data is available from Stallard (2025a). The ion winds measurements used in comparison to our study are available from Stallard (2025c). In addition, the processed data cubes for the individual physical parameters, the outputs from Smith 2011, along with python code to produce the figures in the paper are provided in Stallard (2025b).

Inclusion in Global Research Statement

A clear understanding was reached among collaborators with regard to their roles, responsibilities and conduct throughout the research cycle, from study design through to study implementation, review and dissemination.

Conflict of Interest Statement

The authors have no conflicts of interest to disclose.

Acknowledgments

T.S. and E.M.T. were supported by the STFC Consolidated Grant (ST/W00089X/1). H.M. was supported by the STFC James Webb Fellowship (ST/W001527/2). L.M. acknowledges support from Program number JWST-GO-05308.001-A provided through

a grant from the Space Telescope Science Institute under NASA contract NAS5-03127. J.O'D. was supported by the STFC Ernest Rutherford Fellowship (ST/X003426/1). R.E.J. is supported by NERC grant NE/W002914/1. P.I.T. was supported by a STFC PhD studentship (ST/X508548/2). K.L.K. was supported by a Northumbria University Research Studentship. SVB was supported by STFC grant ST/Y002393/1.

References

Agiwal, O., Hunt, G. J., Dougherty, M. K., Cowley, S. W. H., & Provan, G. (2020). Modeling the temporal variability in saturn's magnetotail current sheet from the cassini f-ring orbits. *Journal of Geophysical Research: Space Physics*, *125*(3). Retrieved from `https://agupubs.onlinelibrary.wiley.com/doi/abs/10.1029/2019JA027371` doi: https://doi.org/10.1029/2019JA027371

Agiwal, O., Masters, A., Hunt, G. J., & Dougherty, M. K. (2022, June). The Contribution of Planetary Period Oscillations Toward Circulation and Mass Loss in Saturn's Magnetosphere. *Journal of Geophysical Research (Space Physics)*, *127*(6), e30439. doi: 10.1029/2022JA030439

Andrews, D., Cowley, S., Dougherty, M., & Provan, G. (2010). Magnetic field oscillations near the planetary period in Saturn's equatorial magnetosphere: Variation of amplitude and phase with radial distance and local time. *Journal of Geophysical Research: Space Physics*, *115*(A4).

Andrews, D. J., Bunce, E. J., Cowley, S. W. H., Dougherty, M. K., Provan, G., & Southwood, D. J. (2008, September). Planetary period oscillations in Saturn's magnetosphere: Phase relation of equatorial magnetic field oscillations and Saturn kilometric radiation modulation. *Journal of Geophysical Research (Space Physics)*, *113*(A9), A09205. doi: 10.1029/2007JA012937

Azari, A. R., Jia, X., Liemohn, M. W., Hospodarsky, G. B., Provan, G., Ye, S. Y., ... Mitchell, D. G. (2019, March). Are Saturn's Interchange Injections Organized by Rotational Longitude? *Journal of Geophysical Research (Space Physics)*, *124*(3), 1806-1822. doi: 10.1029/2018JA026196

Bader, A., Badman, S., Cowley, S., Yao, Z., Ray, L. C., Kinrade, J., ... others (2019). The dynamics of Saturn's main aurorae. *Geophysical Research Letters*, *46*(17-18), 10283–10294.

Bader, A., Badman, S., Kinrade, J., Cowley, S., Provan, G., & Pryor, W. (2018). Statistical Planetary Period Oscillation Signatures in Saturn's UV Auroral Intensity. *Journal of Geophysical Research: Space Physics*, *123*(10), 8459–8472.

Badman, S. V., Achilleos, N., Arridge, C. S., Baines, K. H., Brown, R. H., Bunce, E. J., ... Tao, C. (2012, January). Cassini observations of ion and electron beams at Saturn and their relationship to infrared auroral arcs. *Journal of Geophysical Research (Space Physics)*, *117*(A1), A01211. doi: 10.1029/2011JA017222

Badman, S. V., Andrews, D. J., Cowley, S., Lamy, L., Provan, G., Tao, C., ... others (2012). Rotational modulation and local time dependence of Saturn's infrared H_3^+ auroral intensity. *Journal of Geophysical Research: Space Physics*, *117*(A9).

Bradley, T. J., Cowley, S. W. H., Bunce, E. J., Smith, A. W., Jackman, C. M., & Provan, G. (2018, November). Planetary Period Modulation of Reconnection Bursts in Saturn's Magnetotail. *Journal of Geophysical Research (Space Physics)*, *123*(11), 9476-9507. doi: 10.1029/2018JA025932

Brooks, E. L., Fernandez, C., & Pontius, D. H. (2019, October). Saturn's Multiple, Variable Periodicities: A Dual-Flywheel Model of Thermosphere-Ionosphere-Magnetosphere Coupling. *Journal of Geophysical Research (Space Physics)*, *124*(10), 7820-7836. doi: 10.1029/2019JA026870

Brown, Z., Koskinen, T., Müller-Wodarg, I., West, R., Jouchoux, A., & Esposito, L. (2020, April). A pole-to-pole pressure-temperature map of Saturn's thermo-

sphere from Cassini Grand Finale data. *Nature Astronomy*, *4*, 872-879. doi: 10.1038/s41550-020-1060-0

Bunce, E., Arridge, C., Clarke, J., Coates, A., Cowley, S., Dougherty, M. K., ... others (2008). Origin of Saturn's aurora: Simultaneous observations by Cassini and the Hubble Space Telescope. *Journal of Geophysical Research: Space Physics*, *113*(A9).

Burke, B. F., & Franklin, K. L. (1955, June). Observations of a Variable Radio Source Associated with the Planet Jupiter. *Journal of Geophysical Research*, *60*(2), 213-217. doi: 10.1029/JZ060i002p00213

Bushouse, H., Eisenhamer, J., Dencheva, N., Davies, J., Greenfield, P., Morrison, J., ... Filippazzo, J. (2025, April). *JWST Calibration Pipeline.* Zenodo. doi: 10.5281/zenodo.15178003

Carbary, J. F., Hedman, M. M., Hill, T. W., Jia, X., Kurth, W., Lamy, L., & Provan, G. (2018). The Mysterious Periodicities of Saturn. In K. H. Baines, F. M. Flasar, N. Krupp, & T. Stallard (Eds.), *Saturn in the 21st century* (p. 97-125). doi: 10.1017/9781316227220.005

Chowdhury, M. N. (2022). *Infrared Observations of Saturn's Aurorae, Ionosphere and Thermosphere* (Unpublished doctoral dissertation). University of Leicester.

Chowdhury, M. N., Stallard, T. S., Baines, K., Provan, G., Melin, H., Hunt, G. J., ... others (2022). Saturn's Weather-Driven Aurorae Modulate Oscillations in the Magnetic Field and Radio Emissions. *Geophysical Research Letters*, *49*(3), e2021GL096492.

Chowdhury, M. N., Stallard, T. S., Melin, H., & Johnson, R. E. (2019). Exploring key characteristics in Saturn's infrared auroral emissions using VLT-CRIRES: H_3^+ intensities, ion line-of-sight velocities, and rotational temperatures. *Geophysical Research Letters*. doi: 10.1029/2019GL083250

Clarke, J., Nichols, J., Gérard, J.-C., Grodent, D., Hansen, K., Kurth, W., ... others (2009). Response of Jupiter's and Saturn's auroral activity to the solar wind. *Journal of Geophysical Research: Space Physics*, *114*(A5).

Cowley, S. W. H., Achilleos, N., Bradley, T. J., Provan, G., Bunce, E. J., & Hunt, G. J. (2020, September). Seasonal Dependence of the Magnetospheric Drag Torque on Saturn's Northern and Southern Polar Thermospheres and its Relation to the Periods of Planetary Period Oscillations. *Journal of Geophysical Research (Space Physics)*, *125*(9), e28247. doi: 10.1029/2020JA028247

Cowley, S. W. H., & Provan, G. (2016, July). Planetary period oscillations in Saturn's magnetosphere: Further comments on the relationship between post-equinox properties deduced from magnetic field and Saturn kilometric radiation measurements. *Icarus*, *272*, 258-276. doi: 10.1016/j.icarus.2016.02.051

Cowley, S. W. H., & Provan, G. (2017, June). Planetary period modulations of Saturn's magnetotail current sheet during northern spring: Observations and modeling. *Journal of Geophysical Research (Space Physics)*, *122*(6), 6049-6077. doi: 10.1002/2017JA023993

Cowley, S. W. H., & Provan, G. (2021, August). Physical Origin of Recurrent Magnetic Dipolarization Events in Saturn's Equatorial Plasma Sheet. *Journal of Geophysical Research (Space Physics)*, *126*(8), e29444. doi: 10.1029/2021JA029444

Drossart, P., Maillard, J. P., Caldwell, J., Kim, S. J., Watson, J. K. G., Majewski, W. A., ... Wagener, R. (1989, August). Detection of H_3^+ on Jupiter. *Nature*, *340*(6234), 539-541. doi: 10.1038/340539a0

Dungey, J. W. (1961). Interplanetary magnetic field and the auroral zones. *Physical Review Letters*, *6*(2), 47.

Fischer, G., Gurnett, D. A., Kurth, W. S., Ye, S.-Y., & Groene, J. B. (2015, July). Saturn kilometric radiation periodicity after equinox. *Icarus*, *254*, 72-91. doi: 10.1016/j.icarus.2015.03.014

Fletcher, L. N., Orton, G. S., Sinclair, J. A., Guerlet, S., Read, P. L., Antuñano, A., ... Calcutt, S. B. (2018, September). A hexagon in Saturn's northern stratosphere surrounding the emerging summertime polar vortex. *Nature Communications*, *9*, 3564. doi: 10.1038/s41467-018-06017-3

Galand, M., Moore, L., Mueller-Wodarg, I., Mendillo, M., & Miller, S. (2011). Response of Saturn's auroral ionosphere to electron precipitation: Electron density, electron temperature, and electrical conductivity. *Journal of Geophysical Research: Space Physics*, *116*(A9).

Geballe, T., Jagod, M.-F., & Oka, T. (1993). Detection of H_3^+ infrared emission lines in Saturn. *The Astrophysical Journal*, *408*, L109–L112.

Gérard, J. C., Bonfond, B., Gustin, J., Grodent, D., Clarke, J. T., Bisikalo, D., & Shematovich, V. (2009, January). Altitude of Saturn's aurora and its implications for the characteristic energy of precipitated electrons. *Geophysical Research Letters*, *36*(2), L02202. doi: 10.1029/2008GL036554

Gold, T. (1968, May). Rotating Neutron Stars as the Origin of the Pulsating Radio Sources. *Nature*, *218*(5143), 731-732. doi: 10.1038/218731a0

Gurnett, D., Groene, J., Persoon, A., Menietti, J., Ye, S.-Y., Kurth, W., ... Lecacheux, A. (2010). The reversal of the rotational modulation rates of the north and south components of saturn kilometric radiation near equinox. *Geophysical Research Letters*, *37*(24).

Gurnett, D., Lecacheux, A., Kurth, W., Persoon, A., Groene, J., Lamy, L., ... Carbary, J. (2009). Discovery of a north-south asymmetry in Saturn's radio rotation period. *Geophysical Research Letters*, *36*(16).

Gurnett, D., Persoon, A., Kurth, W., Groene, J., Averkamp, T., Dougherty, M., & Southwood, D. (2007). The variable rotation period of the inner region of Saturn's plasma disk. *Science*, *316*(5823), 442–445.

Helled, R., Galanti, E., & Kaspi, Y. (2015, April). Saturn's fast spin determined from its gravitational field and oblateness. *Nature*, *520*(7546), 202-204. doi: 10.1038/nature14278

Hunt, G. J., Bunce, E. J., Cao, H., Cowley, S. W. H., Dougherty, M. K., Provan, G., & Southwood, D. J. (2020, May). Saturn's Auroral Field-Aligned Currents: Observations From the Northern Hemisphere Dawn Sector During Cassini's Proximal Orbits. *Journal of Geophysical Research (Space Physics)*, *125*(5), e27683. doi: 10.1029/2019JA027683

Hunt, G. J., Cowley, S., Provan, G., Bunce, E., Alexeev, I., Belenkaya, E., ... Coates, A. (2015). Field-aligned currents in Saturn's northern nightside magnetosphere: Evidence for interhemispheric current flow associated with planetary period oscillations. *Journal of Geophysical Research: Space Physics*, *120*(9), 7552–7584.

Hunt, G. J., Cowley, S. W., Provan, G., Bunce, E. J., Alexeev, I. I., Belenkaya, E. S., ... Coates, A. J. (2014). Field-aligned currents in Saturn's southern nightside magnetosphere: Subcorotation and planetary period oscillation components. *Journal of Geophysical Research: Space Physics*, *119*(12), 9847–9899.

Hunt, G. J., Provan, G., Bradley, T. J., Cowley, S. W. H., Dougherty, M. K., & Roussos, E. (2022, June). The Response of Saturn's Dawn Field-Aligned Currents to Magnetospheric and Ring Current Conditions During Cassini's Proximal Orbits: Evidence for a Region 2 Response at Saturn. *Journal of Geophysical Research (Space Physics)*, *127*(6), e29852. doi: 10.1029/2021JA029852

Iñurrigarro, P., Medvedev, A. S., Müller-Wodarg, I. C. F., & Moore, L. (2024, October). Aurorally Driven Supersonic Gravity Waves in Saturn's Atmosphere. *Geophysical Research Letters*, *51*(19), e2024GL110883. doi: 10.1029/2024GL110883

Jackman, C. M., Provan, G., & Cowley, S. W. H. (2016, April). Reconnection events in Saturn's magnetotail: Dependence of plasmoid occurrence on planetary period oscillation phase. *Journal of Geophysical Research (Space Physics)*,

121(4), 2922-2934. doi: 10.1002/2015JA021985

Jakobsen, P., Ferruit, P., Alves de Oliveira, C., Arribas, S., Bagnasco, G., Barho, R., ... Zincke, C. (2022, May). The Near-Infrared Spectrograph (NIRSpec) on the James Webb Space Telescope. I. Overview of the instrument and its capabilities. *Astronomy and Astrophysics*, *661*, A80. doi: 10.1051/0004-6361/202142663

Jia, X., Kivelson, M. G., & Gombosi, T. I. (2012). Driving Saturn's magnetospheric periodicities from the upper atmosphere/ionosphere. *Journal of Geophysical Research: Space Physics*, *117*(A4).

Johnson, R. E., Melin, H., Stallard, T. S., Tao, C., Nichols, J. D., & Chowdhury, M. N. (2018). Mapping H_3^+ Temperatures in Jupiter's Northern Auroral Ionosphere Using VLT-CRIRES. *Journal of Geophysical Research: Space Physics*, *123*(7), 5990–6008.

Kaiser, M. L., Desch, M. D., Warwick, J. W., & Pearce, J. B. (1980). Voyager detection of nonthermal radio emission from Saturn. *Science*, *209*(4462), 1238–1240.

Kinrade, J., Badman, S. V., Provan, G., Cowley, S., Lamy, L., & Bader, A. (2018). Saturn's northern auroras and their modulation by rotating current systems during late northern spring in early 2014. *Journal of Geophysical Research: Space Physics*, *123*(8), 6289–6306.

Koskinen, T. T., Sandel, B. R., Yelle, R. V., Strobel, D. F., Müller-Wodarg, I. C. F., & Erwin, J. T. (2015, November). Saturn's variable thermosphere from Cassini/UVIS occultations. *Icarus*, *260*, 174-189. doi: 10.1016/j.icarus.2015.07.008

Koskinen, T. T., Strobel, D. F., & Brown, Z. (2021, July). An empirical model of the Saturn thermosphere. *Icarus*, *362*, 114396. doi: 10.1016/j.icarus.2021.114396

Krupp, N., Lagg, A., Woch, J., Krimigis, S. M., Livi, S., Mitchell, D. G., ... Dougherty, M. K. (2005, July). The Saturnian plasma sheet as revealed by energetic particle measurements. *Geophysical Research Letters*, *32*(20), L20S03. doi: 10.1029/2005GL022829

Kurth, W., Averkamp, T., Gurnett, D., Groene, J., & Lecacheux, A. (2008). An update to a saturnian longitude system based on kilometric radio emissions. *Journal of Geophysical Research: Space Physics*, *113*(A5).

Lam, H. A., Achilleos, N., Miller, S., Tennyson, J., Trafton, L. M., Geballe, T. R., & Ballester, G. E. (1997). A baseline spectroscopic study of the infrared auroras of Jupiter. *Icarus*, *127*(2), 379–393.

Lamy, L., Prangé, R., Pryor, W., Gustin, J., Badman, S., Melin, H., ... Brandt, P. (2013). Multispectral simultaneous diagnosis of Saturn's aurorae throughout a planetary rotation. *Journal of Geophysical Research: Space Physics*, *118*(8), 4817–4843.

Mankovich, C., Marley, M. S., Fortney, J. J., & Movshovitz, N. (2019, January). Cassini Ring Seismology as a Probe of Saturn's Interior. I. Rigid Rotation. *Astrophysical Journal*, *871*(1), 1. doi: 10.3847/1538-4357/aaf798

Mauk, B. H., Haggerty, D. K., Paranicas, C., Clark, G., Kollmann, P., Rymer, A. M., ... Valek, P. (2017, September). Discrete and broadband electron acceleration in Jupiter's powerful aurora. *Nature*, *549*(7670), 66-69. doi: 10.1038/nature23648

Melin, H. (2020, December). The upper atmospheres of Uranus and Neptune. *Philosophical Transactions of the Royal Society of London Series A*, *378*(2187), 20190478. doi: 10.1098/rsta.2019.0478

Melin, H. (2025). h3ppy: An open-source python package for modelling and fitting h_3^+ spectra. *Journal of Open Source Software*, *10*(107), 7536. Retrieved from `https://doi.org/10.21105/joss.07536` doi: 10.21105/joss.07536

Melin, H., Miller, S., Stallard, T. S., Smith, C., & Grodent, D. (2006). Estimated

energy balance in the jovian upper atmosphere during an auroral heating event. *Icarus*, *181*(1), 256–265. doi: 10.1016/j.icarus.2005.11.004

Melin, H., Moore, L., Fletcher, L. N., Hammel, H. B., O'Donoghue, J., Stallard, T. S., ... Knowles, K. L. (2025, March). Discovery of H_3^+ and infrared aurorae at Neptune with JWST. *Nature Astronomy*. doi: 10.1038/s41550-025-02507-9

Melin, H., Stallard, T., Miller, S., Trafton, L. M., Encrenaz, T., & Geballe, T. R. (2011, March). Seasonal Variability in the Ionosphere of Uranus. *The Astrophysical Journal*, *729*(2), 134. doi: 10.1088/0004-637X/729/2/134

Melin, H., Stallard, T. S., Miller, S., Gustin, J., Galand, M., Badman, S. V., ... Baines, K. (2011). Simultaneous Cassini VIMS and UVIS observations of Saturn's southern aurora: Comparing emissions from H, H2 and H3+ at a high spatial resolution. *Geophysical research letters*, *38*(15).

Melin, H., Stallard, T. S., O'Donoghue, J., Badman, S. V., Miller, S., & Blake, J. (2013). On the anticorrelation between H_3^+ temperature and density in giant planet ionospheres. *Monthly Notices of the Royal Astronomical Society*, *438*(2), 1611–1617.

Melin, H., Stallard, T. S., O'Donoghue, J., Moore, L., Tiranti, P. I., Knowles, K. L., ... Thomas, E. (2025, August). Temporal Variability of the Northern Infrared Aurora of Jupiter as Captured by JWST. *Journal of Geophysical Research (Space Physics)*, *130*(8), e2025JA034261. doi: 10.1029/2025JA034261

Miller, S., Joseph, R. D., & Tennyson, J. (1990, September). Infrared Emissions of H 3 + in the Atmosphere of Jupiter in the 2.1 and 4.0 Micron Region. *Astrophysical Journal Letters*, *360*, L55. doi: 10.1086/185811

Miller, S., Stallard, T. S., Tennyson, J., & Melin, H. (2013). Cooling by H_3^+ emission. *The Journal of Physical Chemistry A*, *117*(39), 9770–9777.

Miller, S., Tennyson, J., Geballe, T. R., & Stallard, T. S. (2020, July). Thirty years of H_3^+ astronomy. *Reviews of Modern Physics*, *92*(3), 035003. doi: 10.1103/RevModPhys.92.035003

Moore, L., O'Donoghue, J., Müller-Wodarg, I., Galand, M., & Mendillo, M. (2015, January). Saturn ring rain: Model estimates of water influx into Saturn's atmosphere. *Icarus*, *245*, 355-366. doi: 10.1016/j.icarus.2014.08.041

Morooka, M. W., Modolo, R., Wahlund, J. E., André, M., Eriksson, A. I., Persoon, A. M., ... Dougherty, M. (2009, July). The electron density of Saturn's magnetosphere. *Annales Geophysicae*, *27*(7), 2971-2991. doi: 10.5194/angeo-27-2971-2009

Müller-Wodarg, I. C. F., Koskinen, T. T., Moore, L., Serigano, J., Yelle, R. V., Hörst, S., ... Mendillo, M. (2019, March). Atmospheric Waves and Their Possible Effect on the Thermal Structure of Saturn's Thermosphere. *Geophysical Research Letters*, *46*(5), 2372-2380. doi: 10.1029/2018GL081124

Mura, A., Moirano, A., Hue, V., Castagnoli, C., Migliorini, A., Altieri, F., ... Sordini, R. (2025, February). Vertical and Temporal H_3^+ Structure at the Auroral Footprint of Io. *The Planetary Science Journal*, *6*(2), 49. doi: 10.3847/PSJ/ada6aa

Nichols, J. D., & Cowley, S. W. H. (2022, January). Relation of Jupiter's Dawnside Main Emission Intensity to Magnetospheric Currents During the Juno Mission. *Journal of Geophysical Research (Space Physics)*, *127*(1), e30040. doi: 10.1029/2021JA030040

Nichols, J. D., King, O. R. T., Clarke, J. T., de Pater, I., Fletcher, L. N., Melin, H., ... Yeoman, T. K. (2025, May). Dynamic infrared aurora on Jupiter. *Nature Communications*, *16*(1), 3907. doi: 10.1038/s41467-025-58984-z

O'Donoghue, J., Melin, H., Stallard, T. S., Provan, G., Moore, L., Badman, S. V., ... Blake, J. S. D. (2016, January). Ground-based observations of Saturn's auroral ionosphere over three days: Trends in H_3^+ temperature, density and emission with Saturn local time and planetary period oscillation. *Icarus*, *263*,

44-55. doi: 10.1016/j.icarus.2015.04.018

O'Donoghue, J., Melin, H., Stallard, T. S., Provan, G., Moore, L., Badman, S. V., ... Blake, J. S. (2016). Ground-based observations of Saturn's auroral ionosphere over three days: Trends in H_3^+ temperature, density and emission with Saturn local time and planetary period oscillation. *Icarus*, *263*, 44–55.

O'Donoghue, J., Moore, L., Bhakyapaibul, T., Melin, H., Stallard, T., Connerney, J. E. P., & Tao, C. (2021, August). Global upper-atmospheric heating on Jupiter by the polar aurorae. *Nature*, *596*(7870), 54-57. doi: 10.1038/s41586-021-03706-w

O'Donoghue, J., Moore, L., Melin, H., Stallard, T. S., Kurth, W. S., Owens, M., ... Murakami, G. (2025, April). Sub-Auroral Heating at Jupiter Following a Solar Wind Compression. *Geophysical Reseach Letters*, *52*(7), 2024GL113751. doi: 10.1029/2024GL113751

O'Donoghue, J., Stallard, T. S., Melin, H., Cowley, S. W., Badman, S. V., Moore, L., ... Blake, J. S. (2014). Conjugate observations of Saturn's northern and southern H_3^+ aurorae. *Icarus*, *229*, 214–220.

O'Donoghue, J., Stallard, T. S., Melin, H., Jones, G. H., Cowley, S. W. H., Miller, S., ... Blake, J. S. D. (2013, April). The domination of Saturn's low-latitude ionosphere by ring 'rain'. *Nature*, *496*(7444), 193-195. doi: 10.1038/nature12049

Provan, G., Andrews, D. J., Arridge, C. S., Coates, A. J., Cowley, S. W. H., Cox, G., ... Jackman, C. M. (2012, January). Dual periodicities in planetary-period magnetic field oscillations in Saturn's tail. *Journal of Geophysical Research (Space Physics)*, *117*(A1), A01209. doi: 10.1029/2011JA017104

Provan, G., Andrews, D. J., Cecconi, B., Cowley, S. W. H., Dougherty, M. K., Lamy, L., & Zarka, P. M. (2011, April). Magnetospheric period magnetic field oscillations at Saturn: Equatorial phase "jitter" produced by superposition of southern and northern period oscillations. *Journal of Geophysical Research (Space Physics)*, *116*(A4), A04225. doi: 10.1029/2010JA016213

Provan, G., Bradley, T. J., Bunce, E. J., Cowley, S. W. H., Cao, H., Dougherty, M., ... Tao, C. (2021, March). Saturn's Nightside Ring Current During Cassini's Grand Finale. *Journal of Geophysical Research (Space Physics)*, *126*(3), e28605. doi: 10.1029/2020JA028605

Provan, G., Cowley, S. W. H., Bradley, T. J., Bunce, E. J., Hunt, G. J., Cao, H., & Dougherty, M. K. (2019, November). Magnetic Field Observations on Cassini's Proximal Periapsis Passes: Planetary Period Oscillations and Mean Residual Fields. *Journal of Geophysical Research (Space Physics)*, *124*(11), 8814-8864. doi: 10.1029/2019JA026800

Provan, G., Cowley, S. W. H., Bunce, E. J., Bradley, T. J., Hunt, G. J., Cao, H., & Dougherty, M. K. (2019, January). Variability of Intra-D Ring Azimuthal Magnetic Field Profiles Observed on Cassini's Proximal Periapsis Passes. *Journal of Geophysical Research (Space Physics)*, *124*(1), 379-404. doi: 10.1029/2018JA026121

Provan, G., Cowley, S. W. H., Bunce, E. J., Milan, S. E., Persoon, A. M., & Gurnett, D. A. (2021, September). Planetary Period Oscillations of Saturn's Dayside Equatorial Ionospheric Electron Density Observed on Cassini's Proximal Passes. *Journal of Geophysical Research (Space Physics)*, *126*(9), e29332. doi: 10.1029/2021JA029332

Provan, G., Cowley, S. W. H., Lamy, L., Bunce, E. J., Hunt, G. J., Zarka, P., & Dougherty, M. K. (2016, October). Planetary period oscillations in Saturn's magnetosphere: Coalescence and reversal of northern and southern periods in late northern spring. *Journal of Geophysical Research (Space Physics)*, *121*(10), 9829-9862. doi: 10.1002/2016JA023056

Provan, G., Lamy, L., Cowley, S. W. H., & Bunce, E. J. (2019, February). Planetary Period Oscillations in Saturn's Magnetosphere: Comparison of Magnetic and

SKR Modulation Periods and Phases During Northern Summer to the End of the Cassini Mission. *Journal of Geophysical Research (Space Physics)*, *124*(2), 1157-1172. doi: 10.1029/2018JA026079

Provan, G., Tao, C., Cowley, S. W., Dougherty, M., & Coates, A. (2015). Planetary period oscillations in Saturn's magnetosphere: Examining the relationship between abrupt changes in behavior and solar wind-induced magnetospheric compressions and expansions. *Journal of Geophysical Research: Space Physics*, *120*(11), 9524–9544.

Roberts, K., Moore, L., O'Donoghue, J., Melin, H., Stallard, T., Knowles, K. L., ... Tiranti, P. I. (2025, April). Spatiotemporal Variations of Temperature in Jupiter's Upper Atmosphere. *Planetary Science Journal*, *6*(4), 92. doi: 10.3847/PSJ/adc09b

Salveter, A., Saur, J., Clark, G., & Mauk, B. H. (2022, August). Jovian Auroral Electron Precipitation Budget—A Statistical Analysis of Diffuse, Mono-Energetic, and Broadband Auroral Electron Distributions. *Journal of Geophysical Research (Space Physics)*, *127*(8), e30224. doi: 10.1029/2021JA030224

Sánchez-Lavega, A., Río-Gaztelurrutia, T., Hueso, R., Pérez-Hoyos, S., García-Melendo, E., Antuñano, A., ... Wesley, A. (2014, March). The long-term steady motion of Saturn's hexagon and the stability of its enclosed jet stream under seasonal changes. *Geophysical Research Letters*, *41*(5), 1425-1431. doi: 10.1002/2013GL059078

Sinclair, J. A., Greathouse, T. K., Giles, R. S., Lacy, J., Moses, J., Hue, V., ... Irwin, P. G. J. (2023, April). A High Spatial and Spectral Resolution Study of Jupiter's Mid-infrared Auroral Emissions and Their Response to a Solar Wind Compression. *The Planetary Science Journal*, *4*(4), 76. doi: 10.3847/PSJ/accb95

Smith, C. (2011). A Saturnian cam current system driven by asymmetric thermospheric heating. *Monthly Notices of the Royal Astronomical Society*, *410*(4), 2315–2328.

Smith, C. (2014). On the nature and location of the proposed twin vortex systems in Saturn's polar upper atmosphere. *Journal of Geophysical Research: Space Physics*, *119*(7), 5964–5977.

Smith, C. (2019). Driving planetary period oscillations from the hall conducting layer of saturn's upper atmosphere. *Journal of Geophysical Research: Space Physics*, *124*(8), 6740–6758.

Smith, C. (2021). Saturn's planetary period oscillations: Interhemispheric coupling and enforcement of the 'plasma cam'by vertically propagating atmospheric waves. *Icarus*, *365*, 114501.

Smith, C., & Achilleos, N. (2012). Axial symmetry breaking of Saturn's thermosphere. *Monthly Notices of the Royal Astronomical Society*, *422*(2), 1460–1488.

Smith, C., Ray, L., & Achilleos, N. (2016). A planetary wave model for saturn's 10.7-h periodicities. *Icarus*, *268*, 76–88.

Smith, C. G. A. (2024, June). A new perspective on Saturn's polar vortices: Coupling the thermosphere and stratosphere. *Icarus*, *415*, 116048. doi: 10.1016/j.icarus.2024.116048

Stallard, T. (2025a). *JWST observations of Saturn's auroral region* [Collection]. Harvard Dataverse. Retrieved from `https://doi.org/10.7910/DVN/F7ZMMW` doi: 10.7910/DVN/F7ZMMW

Stallard, T. (2025b). *JWST observations of Saturn's planetary period temperatures.* Harvard Dataverse. Retrieved from `https://doi.org/10.7910/DVN/VJOOTK` doi: 10.7910/DVN/VJOOTK

Stallard, T. (2025c). *Keck observations of Saturn's asymmetric ion wind velocities.* Harvard Dataverse. Retrieved from `https://doi.org/10.7910/DVN/8UMQAX` doi: 10.7910/DVN/8UMQAX

Stallard, T. S., Baines, K. H., Melin, H., Bradley, T. J., Moore, L., O'Donoghue, J., ... others (2019). Local-time averaged maps of H_3^+ emission, temperature and ion winds. *Philosophical Transactions of the Royal Society A*, *377*(2154), 20180405.

Stallard, T. S., Burrell, A. G., Melin, H., Fletcher, L. N., Miller, S., Moore, L., ... Johnson, R. E. (2018, July). Identification of Jupiter's magnetic equator through $H_3{}^+$ ionospheric emission. *Nature Astronomy*, *2*, 773-777. doi: 10.1038/s41550-018-0523-z

Stallard, T. S., Clarke, J. T., Melin, H., Miller, S., Nichols, J. D., O'Donoghue, J., ... Perry, M. (2016). Stability within Jupiter's polar auroral 'Swirl region'over moderate timescales. *Icarus*, *268*, 145–155.

Stallard, T. S., Masters, A., Miller, S., Melin, H., Bunce, E. J., Arridge, C. S., ... Cowley, S. W. (2012). Saturn's auroral/polar H_3^+ infrared emission: The effect of solar wind compression. *Journal of Geophysical Research: Space Physics*, *117*(A12).

Stallard, T. S., Melin, H., Cowley, S. W., Miller, S., & Lystrup, M. B. (2010). Location and magnetospheric mapping of Saturn's mid-latitude infrared auroral oval. *The Astrophysical Journal Letters*, *722*(1), L85.

Stallard, T. S., Melin, H., Miller, S., Badman, S. V., Brown, R. H., & Baines, K. H. (2012). Peak emission altitude of Saturn's H_3^+ aurora. *Geophysical Research Letters*, *39*(15).

Stallard, T. S., Melin, H., Miller, S., O'Donoghue, J., Cowley, S. W., Badman, S. V., ... Baines, K. H. (2012). Temperature changes and energy inputs in giant planet atmospheres: what we are learning from H_3^+. *Phil. Trans. R. Soc. A*, *370*(1978), 5213–5224.

Stallard, T. S., Miller, S., Millward, G., & Joseph, R. D. (2002). On the dynamics of the Jovian ionosphere and thermosphere: II. The measurement of H_3^+ vibrational temperature, column density, and total emission. *Icarus*, *156*(2), 498–514.

Stallard, T. S., Miller, S., Trafton, L. M., Geballe, T. R., & Joseph, R. D. (2004). Ion winds in Saturn's southern auroral/polar region. *Icarus*, *167*(1), 204–211.

Stallard, T. S., Moore, L., Melin, H., Agiwal, O., Chowdhury, M. N., Johnson, R. E., ... Badman, S. V. (2025, September). JWST/NIRSpec Detection of Complex Structures in Saturn's Sub-Auroral Ionosphere and Stratosphere. *Geophysical Research Letters*, *52*(17), e2025GL116491. doi: 10.1029/2025GL116491

Thomsen, M. F., Jackman, C. M., Cowley, S. W. H., Jia, X., Kivelson, M. G., & Provan, G. (2017, January). Evidence for periodic variations in the thickness of Saturn's nightside plasma sheet. *Journal of Geophysical Research (Space Physics)*, *122*(1), 280-292. doi: 10.1002/2016JA023368

Vasyliunas, V. (1983). Plasma distribution and flow. *Physics of the Jovian magnetosphere*, *1*, 395–453.

Villanueva, G. L., Smith, M. D., Protopapa, S., Faggi, S., & Mandell, A. M. (2018, September). Planetary Spectrum Generator: An accurate online radiative transfer suite for atmospheres, comets, small bodies and exoplanets. *Journal of Quantitative Spectroscopy and Radiative Transfer*, *217*, 86-104. doi: 10.1016/j.jqsrt.2018.05.023

Wang, R., Stallard, T. S., Melin, H., Baines, K. H., Achilleos, N., Rymer, A. M., ... Miller, S. (2023, December). Asymmetric Ionospheric Jets in Jupiter's Aurora. *Journal of Geophysical Research (Space Physics)*, *128*(12), e2023JA031861. doi: 10.1029/2023JA031861

Warwick, J. W., Evans, D. R., Peltzer, G. R., Peltzer, R. G., Romig, J. H., Sawyer, C. B., ... Zarka, P. (1989, December). Voyager Planetary Radio Astronomy at Neptune. *Science*, *246*(4936), 1498-1501. doi: 10.1126/science.246.4936.1498

Warwick, J. W., Evans, D. R., Romig, J. H., Sawyer, C. B., Desch, M. D., Kaiser, M. L., ... Zarka, P. (1986, July). Voyager 2 Radio Observations of Uranus.

Science, *233*(4759), 102-106. doi: 10.1126/science.233.4759.102

Yates, J. N., Ray, L. C., Achilleos, N., Witasse, O., & Altobelli, N. (2020, January). Magnetosphere-Ionosphere-Thermosphere Coupling at Jupiter Using a Three-Dimensional Atmospheric General Circulation Model. *Journal of Geophysical Research (Space Physics)*, *125*(1), e26792. doi: 10.1029/2019JA026792

Ye, S.-Y., Fischer, G., Kurth, W. S., Menietti, J. D., & Gurnett, D. A. (2016, December). Rotational modulation of Saturn's radio emissions after equinox. *Journal of Geophysical Research (Space Physics)*, *121*(12), 11,714-11,728. doi: 10.1002/2016JA023281

Yu, S., Hallinan, G., Doyle, J. G., MacKinnon, A. L., Antonova, A., Kuznetsov, A., ... Zhang, Z. H. (2011, January). Modelling the radio pulses of an ultracool dwarf. *Astronomy and Astrophysics*, *525*, A39. doi: 10.1051/0004-6361/201015580

Figure 1.

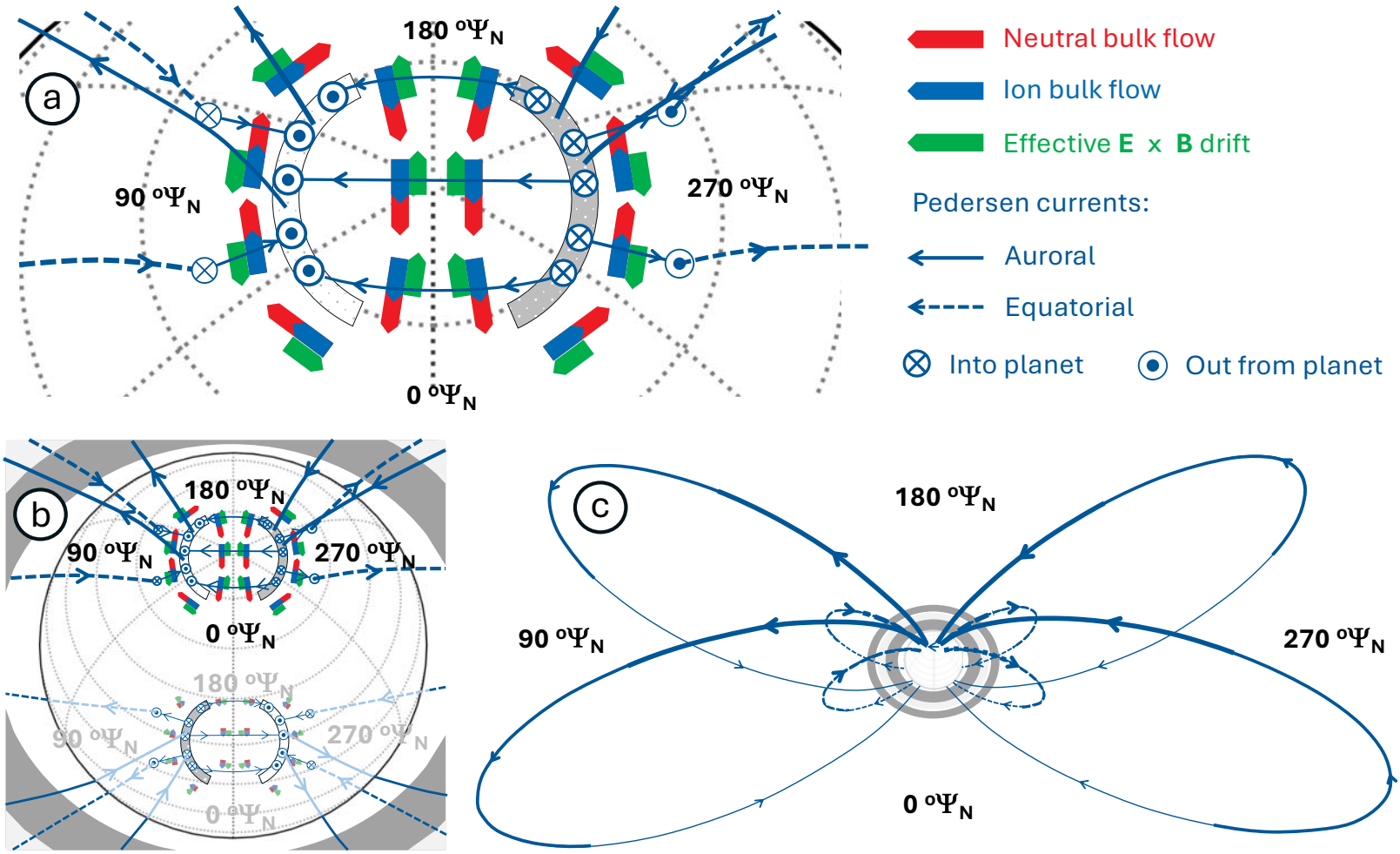
a
180 °Ψ_N
90 °Ψ_N
270 °Ψ_N
0 °Ψ_N
Neutral bulk flow
Ion bulk flow
Effective E x B drift
Pedersen currents:
Auroral
Equatorial
Into planet
Out from planet
b
180 °Ψ_N
90 °Ψ_N
270 °Ψ_N
0 °Ψ_N
c
180 °Ψ_N
90 °Ψ_N
270 °Ψ_N
0 °Ψ_N

Figure 2.

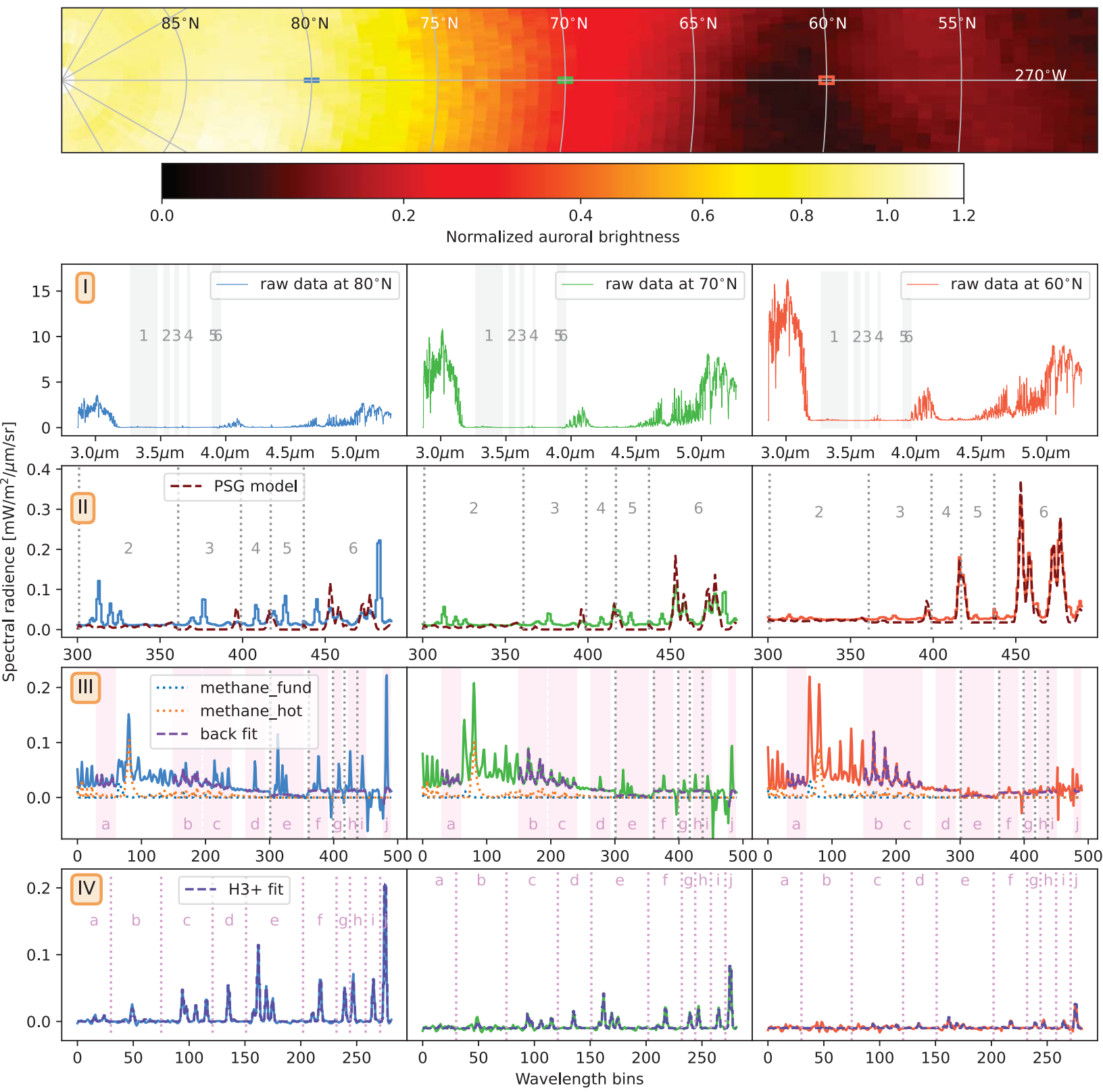
85°N
80°N
75°N
70°N
65°N
60°N
55°N
270°W
0.0
0.2
0.4
0.6
0.8
1.0
1.2
Normalized auroral brightness
I
raw data at 80°N
raw data at 70°N
raw data at 60°N
1 2 3 4 5 6
3.0μm 3.5μm 4.0μm 4.5μm 5.0μm
II
PSG model
2 3 4 5 6
III
methane_fund
methane_hot
back fit
a b c d e f g h i j
IV
H3+ fit
Spectral radience [mW/m²/μm/sr]
Wavelength bins

Figure 3.

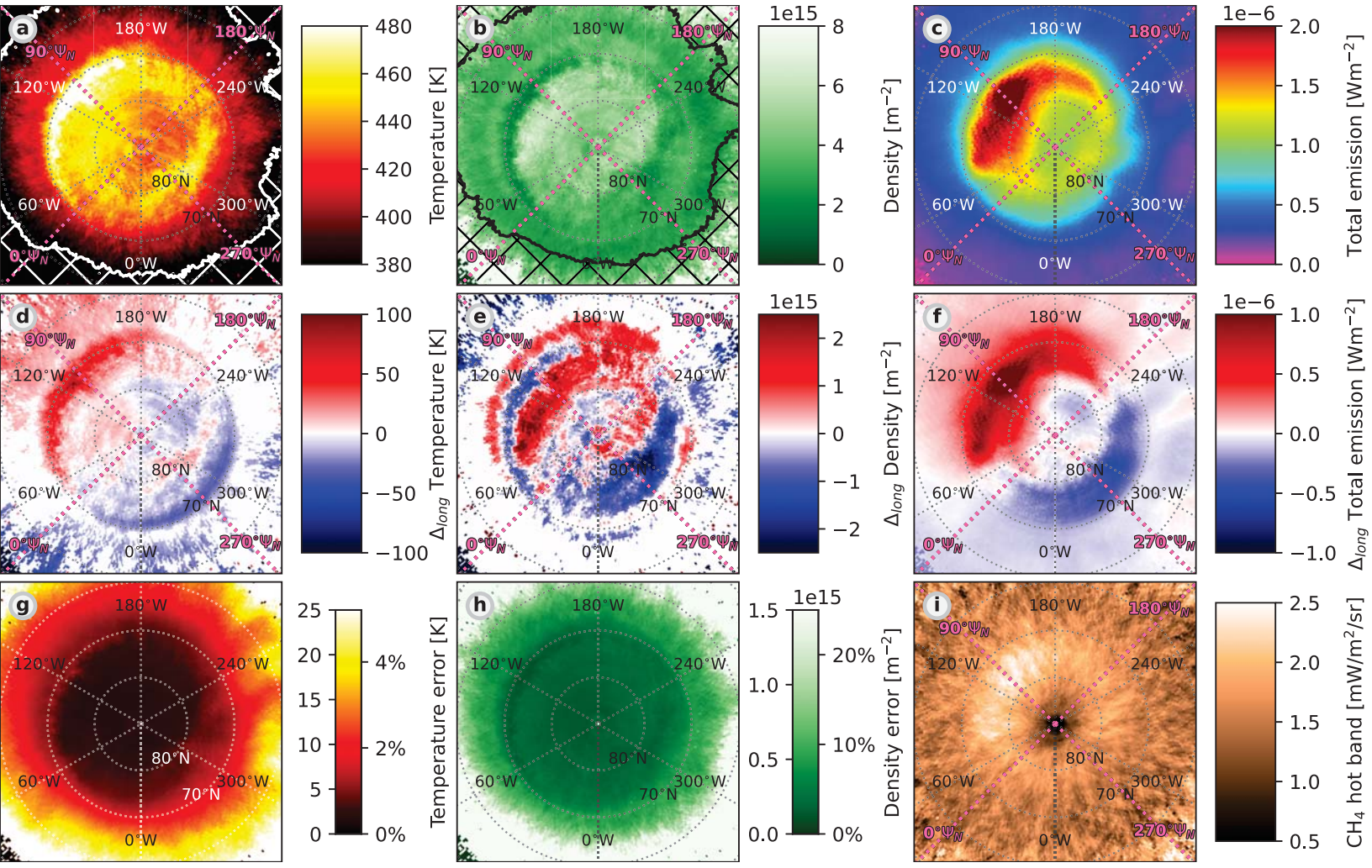
a
b
c
d
e
f
g
h
i
180°W
180°Ψ_N
90°Ψ_N
120°W
240°W
60°W
300°W
80°N
70°N
0°W
0°Ψ_N
270°Ψ_N
Temperature [K]
480
460
440
420
400
380
1e15
8
6
4
2
0
Density [m⁻²]
1e−6
2.0
1.5
1.0
0.5
0.0
Total emission [Wm⁻²]
Δ_long Temperature [K]
100
50
0
−50
−100
Δ_long Density [m⁻²]
−1
−2
Δ_long Total emission [Wm⁻²]
1.0
−0.5
−1.0
Temperature error [K]
25
20
15
10
5
0
4%
2%
0%
1.5
20%
10%
Density error [m⁻²]
2.5
CH4 hot band [mW/m²/sr]

Figure 4.

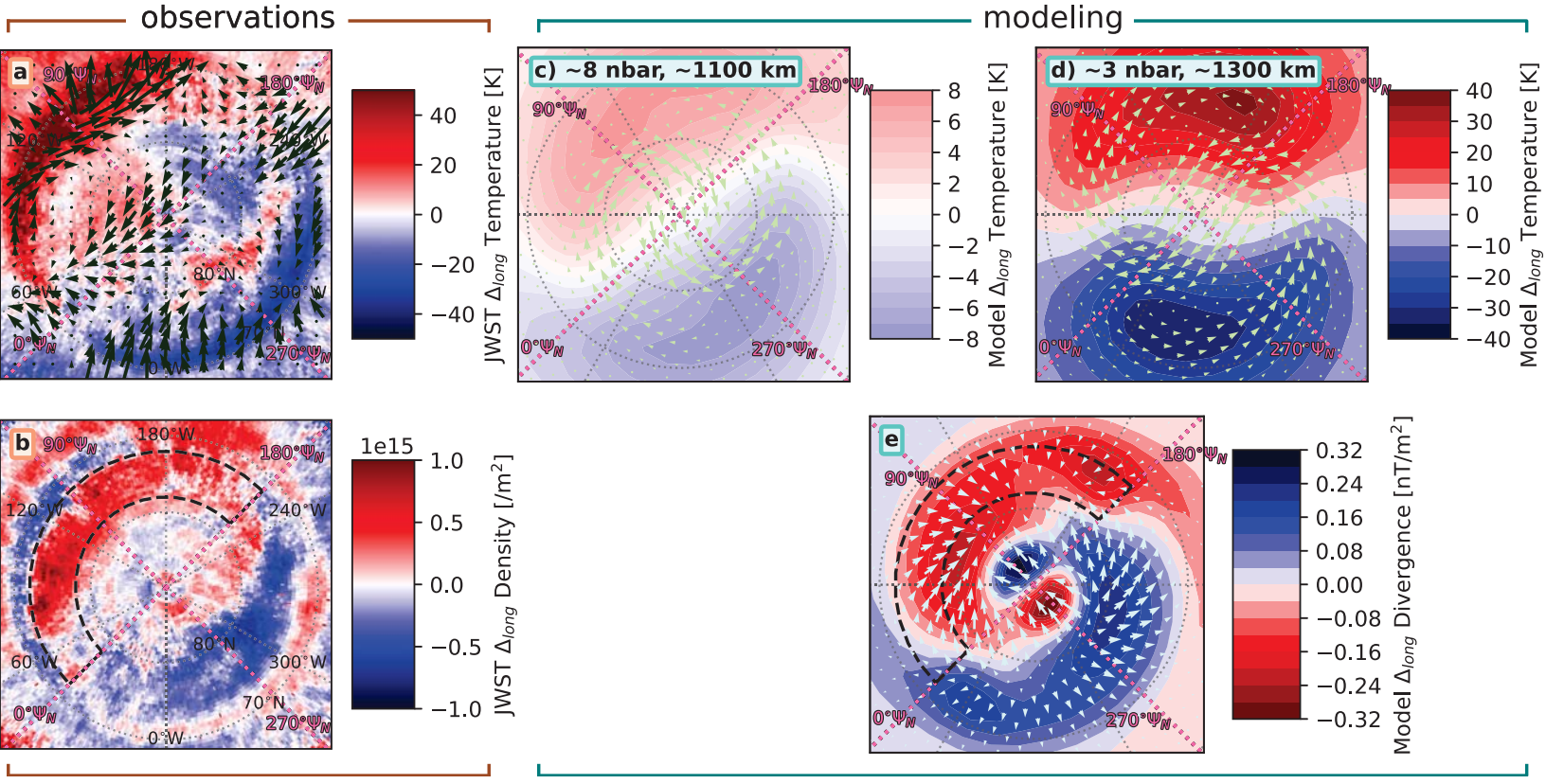
observations
modeling
a
b
c) ~8 nbar, ~1100 km
d) ~3 nbar, ~1300 km
e
JWST Δ_{long} Temperature [K]
Model Δ_{long} Temperature [K]
JWST Δ_{long} Density [/m^2]
Model Δ_{long} Divergence [nT/m^2]
1e15
180°W
90°Ψ_N
180°Ψ_N
0°Ψ_N
270°Ψ_N
120°W
240°W
60°W
300°W
80°N
70°N
0°W